Lipid bilayer array for simultaneous recording of ion channel activities

Ayumi Hirano-Iwata,[1,2,a)] Tomohiro Nasu,[1] Azusa Oshima,[1] Yasuo Kimura,[3] and Michio Niwano[1,3]

[1]*Graduate School of Biomedical Engineering, Tohoku University, 6-6 Aoba, Aramaki, Aoba-ku, Sendai, Miyagi 980-8579, Japan*

[2]*PRESTO, Japan Science and Technology Agency (JST), 4-1-8 Honcho Kawaguchi, Saitama 332-0012, Japan*

[3]*Laboratory for Nanoelectronics and Spintronics, Research Institute of Electrical Communication, Tohoku University, 2-1-1 Katahira, Aoba-ku, Sendai, Miyagi 980-8577, Japan*

(Received 23 April 2012; accepted 25 June 2012; published online 12 July 2012)

This paper describes an array of stable and reduced-solvent bilayer lipid membranes (BLMs) formed in microfabricated silicon chips. BLMs were first vertically formed simultaneously and then turned 90° in order to realize a horizontal BLM array. Since the present BLMs are mechanically stable and robust, the BLMs survive this relatively tough process. Typically, a ~60% yield in simultaneous BLM formation over 9 sites was obtained. Parallel recordings of gramicidin channel activities from different BLMs were demonstrated. The present system has great potential as a platform of BLM-based high throughput drug screening for ion channel proteins. © *2012 American Institute of Physics*. [http://dx.doi.org/10.1063/1.4736263]

Ion-channel proteins regulate the ion flow across cell membranes[1] and are major targets for drug design.[2] Recording ion-channel currents is central to the investigation of the channel function as well as to drug screening applications. Development of high-throughput recording systems for ion-channel proteins is of great importance to improve the experimental efficiency. Several platforms that are capable of simultaneous recordings of ion-channel currents have been proposed, including patch-clamp arrays[3] and bilayer lipid membrane (BLM) arrays.[4–7] Although the patch-clamp method is a golden standard, reconstitution of ion channels in BLMs has an advantage that the researcher can precisely control the composition of the lipid environment, which is not easily manipulated with the patch-clamp method.

Several techniques have been reported as a platform for BLM arrays, such as microfluidic arrays[4,5] and droplet interface bilayer arrays.[6] Each platform offers advantages and disadvantages: for instance, microfluidic arrays allow for easy formation of multiple BLMs, but high surface to volume ratio of the microfluidic systems may be prone to false-negative due to adsorption of test drugs to the walls of microchannels.[8,9] In addition, these approaches are commonly based on BLMs prepared from lipid solutions in unvolatile organic solvents, which are often criticized that some amount of the solvent remains in the central hydrophobic area of the BLMs[10] and likely denatures ion-channel functions. For example, reconstitution of *N*-methyl-D-aspartate receptor channel in droplet interface bilayers[11] resulted in smaller single channel conductance than that reported for solvent-free bilayers[12] in a similar solution condition. In addition, Montal *et al.* recorded activities of acetylcholine receptor channels only when they avoided the use of organic solvents.[13] It is desirable to minimize organic solvent in membranes, though reduction of organic solvent may cause less stable BLMs than solvent-containing BLMs.[14]

The instability of the membranes is the main drawback of BLMs. While various microfabricated devices have been devoted to stabilize bilayers,[15] these devices do not show increased stability except for prolonged lifetimes. Recently, we have reported on mechanically stable BLMs with minimized amount of solvent through the combination of silicon (Si) microfabrication and BLM formation.[16] The BLMs showed tolerance to high applied voltage (±1 V) and mechanical shocks during repetitive solution exchanges, together with long lifetime over 40 h. The key feature that stabilized BLMs is a tapered shape of the aperture edge with a nanometer-scale smoothness, which allows reduction of the stress on the bilayer at the contact with the chip, leading to stable BLMs without using large amount of solvents. In the present study, we have extended this stable BLM device to a 9-site horizontal array format. Simultaneous recording of channel current activities from the multiple BLMs was demonstrated by using a peptidic channel gramicidin. Such BLM array system could find wide-spread applications including drug discovery and development of sophisticated biosensors.

Microapertures with a diameter of 20–60 μm were fabricated in Si chips according to the procedure described in Ref. 16. The fabricated Si chip was silanized by treating with 2% (v/v) cyanopropyldimethylchlorosilane (CPDS) in acetonitrile. BLMs were prepared by the monolayer folding method (Fig. 1).[17] Nine Si chips were set in the middle of a Teflon chamber (Fig. 2). The system was assembled by stacking the bottom component, the Si chips, a perfluoroalkoxy polymer (PFA) sheet, and the top component. Both sides of the chips were precoated with n-hexadecane by dropping a 10-μl aliquot of 0.5% n-hexadecane in chloroform. A ~13-ml portion of 2.0 M KCl solution containing 10 mM HEPES/KOH (*p*H 7.4) was added to each compartment of the chamber. The water level in both compartments was set below the lowest apertures. A 75–100-μl portion of a lipid solution (7 mg/ml L-α-phosphatidylcholine (PC): L-α-phosphatidylethanolamine (PE): cholesterol = 7:1:2 (w/w) dissolved in chloroform/n-hexane (1:1, v/v)) was spread on

a)Author to whom correspondence should be addressed. Electronic mail: ahirano@bme.tohoku.ac.jp. Present address: Graduate School of Biomedical Engineering, Tohoku University, 6-6 Aoba, Aramaki, Aoba-ku, Sendai, Miyagi 980-8579, Japan.

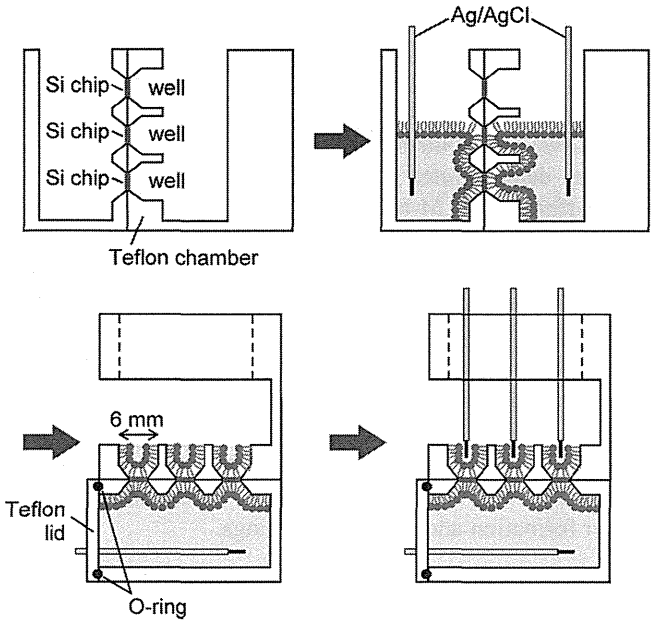

FIG. 1. Procedures for simultaneous BLM formation and rearrangement of the BLMs into a horizontal array format.

the aqueous solutions. After evaporation of the solvent, the water level was gradually raised over apertures to form BLMs at the flow rate of 10 ml/min using a KDS-260 syringe pump (KD Scientific). Incorporation of gramicidin channels into the BLMs was made by adding gramicidin A (Sigma) to the solutions in the both compartments and stirring for 1 h. Relatively, long stirring time was necessary to incorporate gramicidin, as it was more difficult to incorporate gramicidin into the present stable BLMs than into classical folded BLMs.[18] Then, both Ag/AgCl electrodes were plugged off and the opening of the bottom component was covered with a Teflon lid (Fig. 1). A Perfluoro O-ring was used for sealing between the chamber and the lid. Then, the solution in the top component was discarded and the chamber was placed in order that the BLMs were aligned horizontally. Current recordings and capacitance measurements were performed with a sixteen-channel patch-clamp amplifier (Triton$^+$, Tecella). The signal was low-pass filtered at 1 kHz, digitized at 10 kHz, and stored on-line. The data were analyzed using PCLAMP 10.2 software.

In the present system, all the BLMs were formed simultaneously and vertically by the folding method. The amount of an organic solvent required to form the BLMs is much less compared with the painting method,[7] microfluidic systems,[4,5] and droplet interface bilayers.[6,11] This is a great advantage when we consider the application to drug screenings for ion-channel proteins, since fragile ion-channel proteins could hardly tolerate a direct exposure to an organic solvent.[13] On the other hand, the vertical configuration of the BLMs is rather difficult to realize high throughput array systems. As horizontal formats are commonly used for microfluidic BLM arrays,[4,5] a horizontal BLM array is more compatible with high throughput applications. We have designed an experimental setup, where the folded BLMs were first vertically formed and then turned 90° in order to realize a horizontal array of folded BLMs. The volume of each well was ~100 μl, which is suitable for solution handlings and minimizing potential problems associated with drug adsorption to the well surfaces.[8]

Fig. 1 shows our experimental protocol. After simultaneous formation of the BLMs, Ag/AgCl electrodes were plugged off and an aqueous solution in the top compartment was discarded. The BLMs were then laid horizontally and nine Ag/AgCl electrodes were inserted into respective wells. From four to seven BLMs were usually formed with the membrane resistance ranging from 1 to >100 GΩ. The overall probability of keeping BLMs in the horizontal array format, defined as the number of retained BLMs out of total well number examined (=9 × trial number), was found to 61% (60/99) out of 11 trials. Although we did not control possible pressure changes acting on the BLMs during sealing the bottom chamber with a Teflon lid (Fig. 1), which may cause BLM rupture, the observed yield is still higher than that (50%) reported for a microfluidic BLM array.[4] Since the present BLMs were mechanically stable and robust, the BLMs survived such relatively tough process with a moderate yield. The BLMs in the horizontal array format withstood an applied voltage of ±1 V, even when the applied potential was repeatedly switched (Fig. 3), demonstrating that the

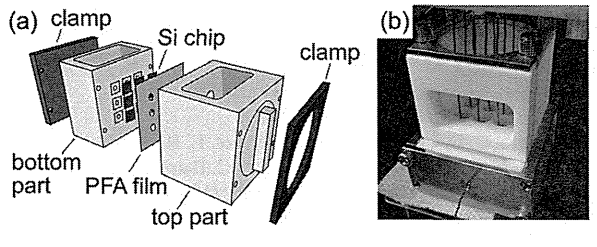

FIG. 2. (a) Drawing of the components of the present system, with the nine BLM sites placed in the Si chips. (b) Photograph of the experimental chamber in the final arrangement.

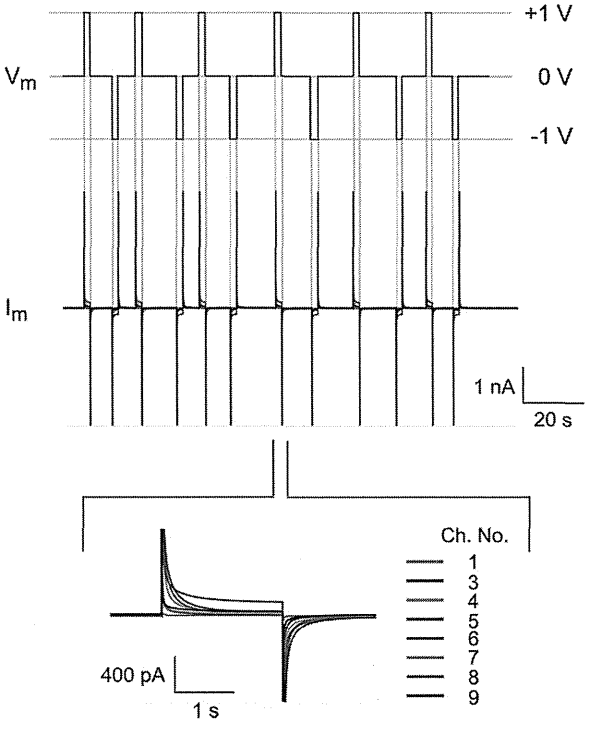

FIG. 3. An example of simultaneously recorded membrane currents (I_m) from eight BLMs when the applied potential (V_m) was repeatedly switched stepwise 0 V → +1 V → 0 V → −1 V → 0 V.

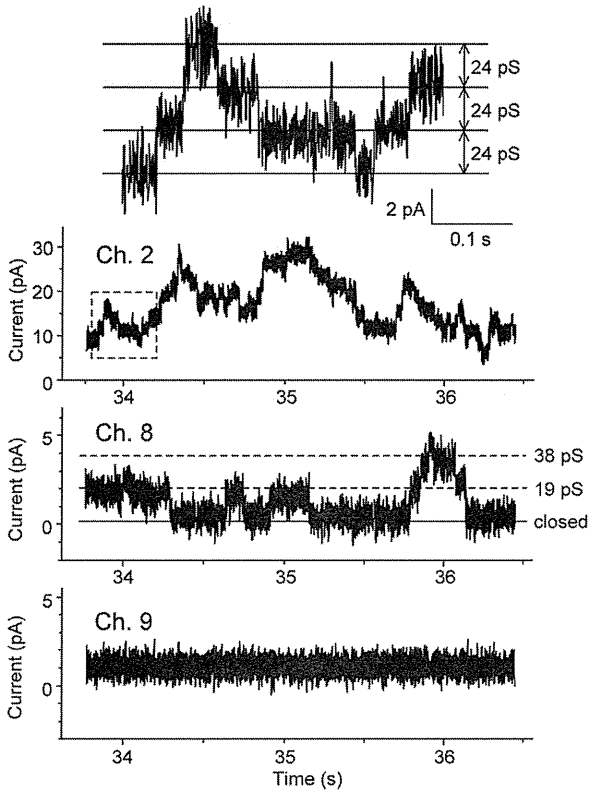

FIG. 4. Simultaneous current recording from three different BLMs. The box in the trace for Ch. 2 highlights the region shown in detail in the top trace.

arrayed BLMs still showed similar stability to those in the previous single BLM device.[16] This voltage (±1 V) is higher than the breakdown voltage (~300–400 mV) reported for BLMs prepared in plastic septa.[19,20]

Fig. 4 shows an example of simultaneous current recordings from three BLMs with and without incorporated gramicidin channels. Gramicidin forms a channel that is permeable to monovalent cations, when gramicidin monomers form a membrane-spanning dimer. At the BLM formed in Ch. 8, distinct stepwise currents were seen with the single-channel conductance of ~19 pS. This level is similar to reported values (19–25 pS in 2.0 M KCl),[16,21–23] confirming the functionality of the present BLMs. With a BLM containing multi channels (Ch. 2), much larger currents with multiple constant steps were observed. The conductance for each step was 24 pS, which is in agreement with gramicidin single-channel conductance. Since more channels were embedded in the BLM in Ch. 2, more frequent open ↔ close transitions were observed with shorter dwell time for each conductance level. No detectable current change was observed for Ch. 9, where no channel was incorporated into the BLM, demonstrating that no interference or crosstalk was detectable among simultaneously recorded BLMs.

In summary, we have succeeded in parallel formation of stable BLMs with minimized amount of solvents in a horizontal array format. All the BLMs were formed simultaneously by the folding method and then rotated 90° to be aligned horizontally. The yield of BLMs in the horizontal array is currently ~60%, but this could be significantly improved by optimizing the rotation process; the water level in the bottom compartment before placing the lid could be more accurately controlled by using automated injection, which will minimize the possible pressure change acting on the BLMs. Simultaneous recording of gramicidin channel activities demonstrates great potential of the present system as a platform of BLM-based high throughput drug screening systems. Although the present study used a 9-site array in order to provide a proof of principle for horizontal array of folded BLMs, in future work, we aim to improve the throughput by increasing the number of BLMs after changing the upper compartment to a detachable one. Combination with automation will also improve the experimental throughput. As the most critical folding process was already automated by using a syringe pump in the present study, we believe that our system can be fully automated including bilayer formation and current recordings.

This work was supported by Grant-in-Aids from Japan Society for the Promotion of Science (Grant Nos. 21350038 and 24350032) and JST (PRESTO). Finally, one (A.O.) of the authors thank the Japan Society for the Promotion of Science for research fellowships.

[1]C. Miller, *Ion Channel Reconstitution* (Plenum, New York, 1986).
[2]J. P. Overington, B. Al-Lazikani, and A. L. Hopkins, Nat. Rev. Drug Discovery **5**, 993 (2006).
[3]C. Py, M. Martina, G. A. Diaz-Quijada, C. C. Luk, D. Martinez, M. W. Denhoff, A. Charrier, T. Comas, R. Monette, A. Krantis, N. I. Syed, and G. A. R. Mealing, Front. Pharmacol. **2**, 1 (2011).
[4]M. Zagnoni, M. E. Sandison, and H. Morgan, Biosens. Bioelectron. **24**, 1235 (2009).
[5]B. Le Pioufle, H. Suzuki, K. V. Tabata, H. Noji, and S. Takeuchi, Anal. Chem. **80**, 328 (2008).
[6]R. Syeda, M. A. Holden, W. L. Hwang, and H. Bayley, J. Am. Chem. Soc. **130**, 15543 (2008).
[7]G. Baaken, M. Sondermann, C. Schlemmer, J. Rühe, and J. C. Behrends, Lab Chip **8**, 938 (2008).
[8]J. Dunlop, M. Bowlby, R. Peri, D. Vasilyev, and R. Arias, Nat. Rev. Drug Discovery **7**, 358 (2008).
[9]L. Guo and H. Guthrie, J. Pharmacol. Toxicol. Methods **52**, 123 (2005).
[10]R. Benz, O. Fröhlich, P. Läuger, and M. Montal, Biochim. Biophys. Acta **394**, 323 (1975).
[11]S. Leptihn, J. R. Thompson, J. C. Ellory, S. J. Tucker, and M. I. Wallace, J. Am. Chem. Soc. **133**, 9370 (2011).
[12]A. Kloda, L. Lua, R. Hall, D. J. Adams, and B. Martinac, Proc. Natl. Acad. Sci. U.S.A. **104**, 1540 (2007).
[13]N. Nelson, R. Anholt, J. Lindstrom, and M. Montal, Proc. Natl. Acad. Sci. U.S.A. **77**, 3057 (1980).
[14]O. V. Batishchev and A. V. Indenbom, Bioelectrochemistry **74**, 22 (2008).
[15]A. Hirano-Iwata, M. Niwano, and M. Sugawara, Trends Anal. Chem. **27**, 512 (2008).
[16]A. Hirano-Iwata, K. Aoto, A. Oshima, T. Taira, R. Yamaguchi, Y. Kimura, and M. Niwano, Langmuir **26**, 1949 (2010).
[17]M. Montal and P. Mueller, Proc. Natl. Acad. Sci. U.S.A. **69**, 3561 (1972).
[18]A. Oshima, A. Hirano-Iwata, T. Nasu, Y. Kimura, and M. Niwano, Micro Nanosyst. **4**, 2 (2012).
[19]M. Mayer, J. K. Kriebel, M. T. Tosteson, and G. M. Whitesides, Biophys. J. **85**, 2684 (2003).
[20]M. C. Peterman, J. M. Ziebarth, O. Braha, H. Bayley, H. A. Fishman, and D. M. Bloom, Biomed. Microdev. **4**, 231 (2002).
[21]O. S. Andersen, Biophys. J. **41**, 119 (1983).
[22]D. D. Busath, C. D. Thulin, R. W. Hendershot, L. R. Phillips, P. Maughan, C. D. Cole, N. C. Bingham, S. Morrison, L. C. Baird, R. J. Hendershot, M. Cotten, and T. A. Cross, Biophys. J. **75**, 2830 (1998).
[23]A. Hirano-Iwata, T. Taira, A. Oshima, Y. Kimura, and M. Niwano, Appl. Phys. Lett. **96**, 213706 (2010).

Society For Biomaterials

In vitro assessment of poly(methylmethacrylate)-based bone cement containing magnetite nanoparticles for hyperthermia treatment of bone tumor

Zhixia Li,[1] Koki Kawamura,[2] Masakazu Kawashita,[2] Tada-aki Kudo,[3] Hiroyasu Kanetaka,[4] Masahiro Hiraoka[5]

[1]College of Chemistry and Chemical Engineering, Guangxi University, Nanning 530004, China
[2]Graduate School of Biomedical Engineering, Tohoku University, Sendai 980-8579, Japan
[3]Division of Oral Physiology, Tohoku University Graduate School of Dentistry, Sendai 980-8575, Japan
[4]Liaison Center for Innovative Dentistry, Graduate School of Dentistry, Tohoku University, Sendai 980-8575, Japan
[5]Department of Radiation Oncology and Image-Applied Therapy, Graduate School of Medicine, Kyoto University, Kyoto 606-8507, Japan

Received 18 September 2011; revised 26 February 2012; accepted 12 March 2012
Published online 24 April 2012 in Wiley Online Library (wileyonlinelibrary.com). DOI: 10.1002/jbm.a.34185

Abstract: Poly(methylmethacrylate) (PMMA)-based cements containing magnetite (C-PMMA/Fe_3O_4) is useful in hyperthermia treatment for bone tumor. We have prepared C-PMMA/Fe_3O_4 by incorporating Fe_3O_4 powders of different diameters (means of 300, 35, and 11 nm) into the polymerization reaction of methyl methacrylate monomer to develop a new bone cement with high heating efficiencies in alternating current (AC) magnetic fields. Further, we have investigated the *in vitro* heating capability of the cements in different AC magnetic fields. The mechanical strength and biocompatibility of the resultant cements were also assessed. Their heat generation strongly depends on the magnetite nanoparticle sizes and applied magnetic fields. The cement containing Fe_3O_4 with mean diameter around 35 nm exhibited the highest heating capability in AC magnetic fields of 120 and 300 Oe at 100 kHz while that with mean diameter around 11 nm exhibited optimum heating capability in AC magnetic fields of 40 Oe at 600 kHz. The incorporation of Fe_3O_4 into cement—30 wt % of the total amount of cement—did not significantly change the compressive strength of cement, and the proliferation of rat fibroblast Rat-1 cells on cement discs was not inhibited. Our investigations are useful for designing new PMMA/Fe_3O_4 bone cement with high heating efficiencies and biocompatibilities for bone tumor treatments. © 2012 Wiley Periodicals, Inc. J Biomed Mater Res Part A: 100A: 2537–2545, 2012.

Key Words: PMMA cement, magnetite, mechanical strength, biocompatibility, hyperthermia

How to cite this article: Li Z, Kawamura K, Kawashita M, Kudo T, Kanetaka H, Hiraoka M. 2012. *In vitro* assessment of poly(methylmethacrylate)-based bone cement containing magnetite nanoparticles for hyperthermia treatment of bone tumor. J Biomed Mater Res Part A 2012:100A:2537–2545.

INTRODUCTION

Bone metastasis occurs most commonly in the spine and typically results in vertebral compression fractures (VCFs). Symptomatic VCFs have been associated with decreased quality of life and increased mortality in the elderly.[1] Acute and chronic pain is a typical symptom of VCFs. Today, several approaches are available for the treatment of painful osteoporotic VCFs, for example, bed rest, analgesia, muscle relaxants, back braces, or a combination of these.[2] However, prolonged bed rest frequently leads to further losses in bone mass and may increase the risk of dementia in elderly patients, while bracing is often poorly tolerated.[3] Recently, vertebroplasty, which involves the percutaneous injection of bone cement into fractured vertebra, has been used as a new treatment method for VCFs. The set or hardened cement stabilizes the fracture, thereby relieving pain.[3,4]

It is well known that magnetic nanoparticles (NPs) can induce heat when placed in an external alternating current (AC) magnetic field. On the basis of this behavior, it has been proposed that bone cement containing magnetic NPs is useful for the hyperthermic treatment of bone tumors.[5–7] In fact, some researchers have attempted to prepare effective Fe_3O_4-containing bone cements in order to treat metastatic bone tumors. Matsumine et al. prepared Fe_3O_4-containing calcium phosphate (Fe_3O_4–CaP) cement[5] and conducted clinical trials to treat 15 patients with metastatic bone lesions by hyperthermic treatment (HT group). The results were then compared with those for eight patients treated by palliative operation (Op group) and 22 patients treated by operations as well as radiotherapy (Op + RT group). The patients in the HT group showed better radiographic outcomes than those in the Op group and no

Correspondence to: Z. Li; e-mail: zhixiali@hotmail.com
Contract grant sponsor: The Scientific Research Foundation of GuangXi University (Grant No. XGZ120081)

significant differences from those in the Op + RT group. In a recent research, we have attempted to add Fe_3O_4 powder with a diameter of around 300 nm into poly(methylmethacrylate) (PMMA) cement.[8] PMMA cement containing 50% Fe_3O_4 exhibited high heating efficiencies even in an AC magnetic field of 120 Oe. Moreover, the Fe_3O_4 NPs were uniformly dispersed in the cement matrix.[8]

However, fine Fe_3O_4 NPs are potentially toxic,[9,10] and moreover, the magnetic field-induced heat easily disperses into the surrounding environment.[11] Hence, bone cement containing a small number of magnetic NPs but with adequate heating capability is desirable for the clinical hyperthermic treatment of bone tumors.

Magnetic NPs induce heat according to two primary mechanisms—hysteresis losses for ferromagnetic NPs and relaxation losses for superparamagnetic NPs—and they depend on the nature of the NPs, such as particle dimensions.[12–14] The heating capability of cement is dominated by two factors: the quantity and dimensions of the employed magnetic NPs. Therefore, we believe that the heating characteristics of magnetic NPs-containing bone cements can be controlled by optimizing the quantity and dimension distributions of the magnetic NPs. In addition, an AC magnetic field generator that can supply magnetic fields with the necessary strength and frequency is also desirable for certain types of magnetic NPs so that more field energy can be transformed into heat. Numerous literatures have revealed the size-dependent relationships of the heat generation of magnetic nanoparticles,[12–14] but we are still unsure of whether the magnetic NPs after incorporation in cements will maintain identical or even similar properties as those before incorporation. Moreover, few researches have been performed to clarify the potential toxicity of magnetic NPs-containing bone cements implanted into defective areas of bones.

In this study, we have prepared several kinds of PMMA-based cements containing Fe_3O_4 NPs (C-PMMA/Fe_3O_4) with different NPs dimensions with the aim of improving their heating capabilities by optimizing the dimension distributions of magnetic nanoparticles. The *in vitro* heat generation of the obtained cements in different AC magnetic fields was measured. The unreacted methyl methacrylate (MMA) monomer concentrations in cement were analyzed by liquid chromatography. The mechanical properties were evaluated by measuring the compressive strength of cements. The *in vitro* biocompatibility of cements was assessed by culturing a Rat-1 fibroblast cell line on cement discs. Our investigations will be useful for designing new PMMA-based cements with high heating efficiencies and good biocompatibilities for conducting hyperthermia treatment for bone tumor.

MATERIALS AND METHODS

Preparation of magnetite nanoparticles

All the chemicals used in our experiments were of analytical reagent grade and were used without further purification. Sodium hydroxide (NaOH), iron (II) chloride ($FeCl_2$), iron (III) chloride ($FeCl_3$), sodium nitrate ($NaNO_3$), and MMA monomer were obtained from Wako Pure Chemical Industries, Osaka, Japan. $FeCl_2$, $FeCl_3$, and NaOH were dissolved in deionized and deoxygenated water. In addition, PMMA beads (Sekisui Plastics, Osaka, Japan) with an average molecular weight of 270 kDa and average particle size of 5 μm were used in our experiment.

Four types of Fe_3O_4 powders with different particle sizes, denoted by REA, OXP, COP, and COP1, were used in this study. REA was commercially available (Wako Pure Chemical Industries) and had a particle size around 300 ± 200 nm. OXP was prepared by an oxidation precipitation method referring to our previous study[15]: in brief, 0.95 g of $NaNO_3$ was added to 168 mL of 0.5*M* NaOH aqueous solution that had been sufficiently deaerated by nitrogen (N_2) gas beforehand. Subsequently, 100 mL of 0.5*M* $FeCl_2$ aqueous solution was added to a $NaNO_3$–NaOH solution with stirring at a rate of 400 rpm in N_2 gas atmosphere. After stirring for 15 min, the solution was subjected to ultrasonic treatments for 10 min and aged at 60°C for 5 h. The precipitates were separated, washed, and dried at 60°C for 12 h. COP was prepared using a co-precipitation method[15] as follows: 75 mL of 0.1*M* $FeCl_2$ solution and 100 mL of 0.1*M* $FeCl_3$ solution were mixed and dropped into 1870 mL of 21 m*M* NaOH solution with stirring. This was followed by ultrasonic treatments for 20 min and aging at 36.5°C for 8 h. The precipitates were separated, washed, and finally dried overnight at 60°C.

However, the quantity of the magnetite NPs (COP) prepared using the above coprecipitation method was too low to prepare sufficient cement samples for statistical assessments of the mechanical and biocompatible properties. Therefore, a modified coprecipitation method[16] was employed to prepare larger quantities of Fe_3O_4 NPs (COP1) with the same particle sizes as those of COP. In brief, COP1 was synthesized as follows: 0.6 mol of $FeCl_2$ and 1.2 mol of $FeCl_3$ were added into 120 mL of 0.5*M* HCl solution, and the mixed solution was rapidly added into 1 L of 1.5*M* NaOH solution that had been deoxygenated by N_2 gas beforehand. Subsequently, the solution was subjected to ultrasonic treatments for 20 min. The resultant precipitates were separated, washed, and dried at 60°C for 12 h under vacuum conditions. In this study, COP1 was not only used to prepare the cement samples for assessing the mechanical and biocompatible properties but also to analyze the residual MMA monomer concentrations in cements.

Preparation of cement samples

Six types of cement samples, C-PMMA, C-REA50, C-REA30, C-OXP50, C-COP30, and C-COP30a, were prepared. Their compositions are listed in Table I. C-PMMA was Fe_3O_4-free cement and used as a control material. On the basis of a previous study, the PMMA powder/MMA liquid weight ratio was maintained at 2:3.[17] Further, as a polymerization initiator, benzoyl peroxide (BPO, Tokyo Chemical Industry, Tokyo, Japan) was added to the powders, and an accelerator *N*, *N*-dimethyl-*p*-toluidine (DMPT, Wako Pure Chemical Industries) was dissolved in the liquid; the concentrations were 4.0 wt % and 2.0 wt % of the MMA monomer, respectively. All the cements were prepared by mixing the powder in the

TABLE I. Compositions of the Cement Samples

Sample	Fe_3O_4 nanoparticle	Powder (wt %)		Liquid (wt %)
		Fe_3O_4	PMMA	MMA
C-PMMA	–	0	40	60
C-REA50	REA	50	20	30
C-REA30	REA	30	28	42
C-OXP50	OXP	50	20	30
C-COP30	COP	30	28	42
C-COP30a	COP1	30	28	42

liquid for 3 min and setting in different molds according to the analysis requirements.

The cement samples for *in vitro* heat studies (C-PMMA, C-REA50, C-REA30, C-OXP50, and C-COP30) and for mechanical property assessments and residual monomer analyses (C-PMMA and C-COP30a), were identically prepared in the following manner. The solid and liquid components given in Table I were mixed for 3 min, and subsequently, the paste was poured into a stainless steel mold containing five holes (diameter = 6 mm; height = 12 mm) and clamped with stainless steel sheets. The cylindrical samples were removed from the mold after they had fully set. Since smaller Fe_3O_4 nanoparticles might be more toxic to cell,[9,10] and moreover easily cause crack of cement samples. Therefore, C-COP30a which contained the smallest Fe_3O_4 nanoparticles, was typically selected to evaluate the mechanical property, residual monomer concentration, and biocompatibility of cement samples.

The cement samples for biocompatibility evaluations (C-PMMA and C-COP30a), were prepared in the following manner. The solid and liquid components given in Table I were mixed for 3 min, and the paste was then poured into a stainless steel mold (diameter = 20 mm; height = 1 mm). Three pieces of cover glasses (diameter = 18 mm) were immediately flatly inlaid into the mold with cement paste in order to increase the weight of the final cement samples. The mold with cement paste and cover glasses was clamped with stainless steel sheets and fixed using a clamp. The cement samples were removed from the mold after they had fully set. The obtained cement discs with cover glasses were sterilized with rubbing alcohol just before conducting the cellular culture test.

Characterization of magnetite nanoparticles and cement samples

The crystalline phases of the magnetite NPs were verified using powder X-ray diffraction (XRD, RINT-2200VL, Rigaku, Tokyo, Japan) with the following experimental settings: X-ray source = Ni-filtered Cu Kα radiation; X-ray power = 40 kV, 40 mA; 2θ scanning rate = 2° min^{-1}; and sampling angle = 0.02°. The particle sizes were observed using a transmission electron microscope (TEM, JEM-2100, JEOL Ltd., Japan). The magnetization properties of the Fe_3O_4 powders and cements were measured using a vibrating sample magnetometer (VSM-5, Toei Industry, Tokyo, Japan) in magnetic fields of 120, 300, and 10,000 Oe at room temperature and 80 Hz frequency.

In vitro heat studies

The *in vitro* heating capabilities of the cement samples were measured in AC magnetic fields of 300 and 120 Oe at a frequency of 100 kHz using an apparatus developed by Kawashita et al.[18]; further, the *in vitro* heating capabilities in an AC magnetic field of 40 Oe at a frequency of 600 kHz were also examined using an apparatus developed by Jeyadevan et al.[19] The changes in the surface temperatures of the cement samples were measured using a fluoroptic thermometer (Model-3000, Luxtron, CA) as a function of time in the AC magnetic fields.

Mechanical properties

The mechanical properties of the cements were evaluated by measuring the compressive strengths of the cement samples in accordance with the standard ISO 5833 procedure. The surfaces of the cement samples prepared according to the method described previously were abraded using #400 sandpaper in order to reduce the stress concentrations at the sample surfaces. A compressive test was conducted using an Instron-type mechanical testing machine (AG-I 50 kN, Shimadzu Co., Kyoto, Japan). For each type of cement sample, we prepared five pieces and tested them at a crosshead displacement rate of 20 mm min^{-1}.

Residual monomer content in cements

The cement samples were weighted and immersed in 5 mL of water in a screw bottle and kept for 7 days at 37°C. The lixiviums were analyzed by Agilent 1200 liquid chromatography using an Eclipse XDB-C18 column (100 mm × 4.6 mm, i.d., 3.5 μm) at column temperature of 30°C. The mobile phase was acetonitrile–water (40:60, v/v), it was eluted at a constant flow rate of 1.0 mL min^{-1}. Totally, 10 μL of lixivium was injected into liquid chromatography. The effluents were monitored using a photodiode array detector at 254 nm. The monomer concentrations in the lixiviums were determined from a least-squares line calibration curve constructed from detector response factors obtained from standard solutions containing 25, 50, 100, and 250 mg L^{-1} monomers. We tested five pieces for each type of cement.

Cell culture and quantification of DNA from cells

Rat fibroblast Rat-1 cells were cultured in Dulbecco's modified Eagle's medium (DMEM, Wako Pure Chemical Industries, Osaka, Japan) containing 10% horse serum (Invitrogen, Carlsbad, CA), 100 units mL^{-1} of penicillin (Meiji Seika Kaisha, Tokyo, Japan), and 100 μg mL^{-1} of streptomycin (Meiji Seika Kaisha). The cells were routinely subcultured every third day in a 60.1 cm^2 culture dish at 37°C in humidified air with 5% CO_2.

A cell suspension consisting of 50,000 Rat-1 cells were seeded over testing cement discs placed on the bottom of 12-well culture plates (five samples per cement). The cells were grown in 1 mL of the medium. The cell proliferation was examined after 1, 4, and 7 days of culture. At each time

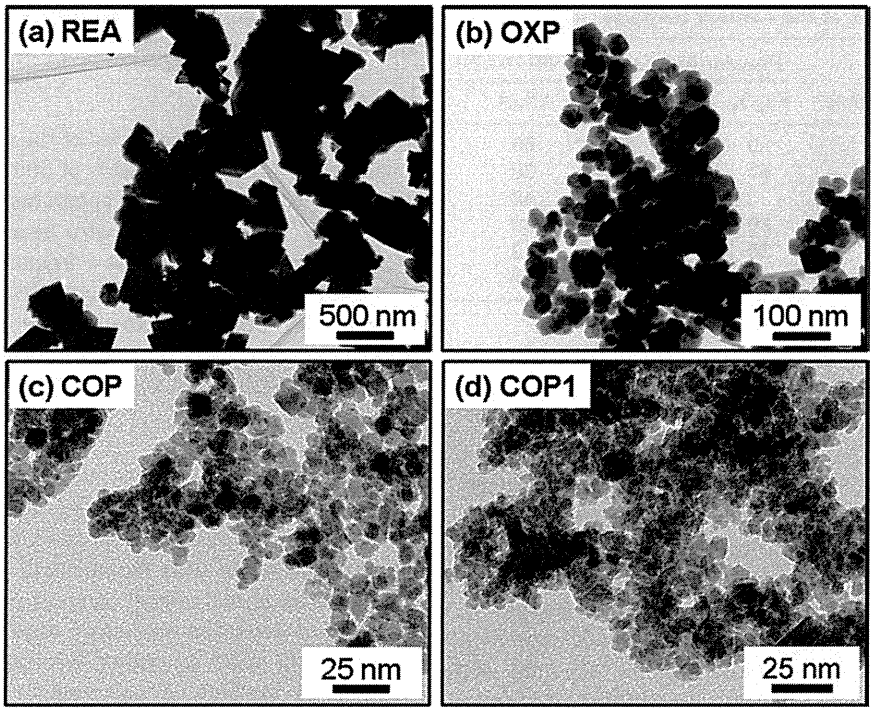

FIGURE 1. TEM photographs of the magnetite powders used in this study.

point, the cement discs were removed from the medium and transferred to a new 12-well culture plate. The total DNA from the incubated cells on the cement discs was extracted using AllPrep DNA/RNA/Protein Mini Kit (Qiagen GmbH, Hilden, Germany) in accordance with the manufacturer's protocol.[20] Following the extraction, the DNA concentrations were measured by absorbance at 260 nm using a spectrophotometer (GeneQuant Pro, GE Healthcare, Buckinghamshire, UK).[21] The values are given as mean DNA-content and derived from five replicates per cement sample.

Statistical analysis

All the results obtained from the compressive strength test, residual MMA monomer content analysis, and cell culture test were expressed as means ± standard deviation. The statistical significance was set at $p < 0.05$ and was calculated with the Student's t test.

RESULTS AND DISCUSSION

Characterization of magnetite nanoparticles and cement samples

Figure 1 shows TEM photographs and Figure 2 shows XRD powder diffraction patterns of the magnetite powders used in this study. REA was composed of cubic NPs, whereas OXP, COP, and COP1 contained nearly spherical NPs. The particle sizes for REA, OXP, COP, and COP1 were 300 ± 200 nm, 35 ± 15 nm, 11.5 ± 3.6 nm, and 5 ± 3 nm, respectively. The XRD patterns of all the powders were similar and verified to be peaks attributable to magnetite (Fe_3O_4).[22]

We initially expected the method reported in literature 16 to produce Fe_3O_4 NPs (COP1) with a size close to that of COP (~10 nm). However, in fact, COP1 was smaller than COP, and this can be attributed to some modifications to the synthesis process; in this study, a larger dose of reactants than that in the literature was used. The stirring strength decreases as the quantity of the reactants increases, thereby slowing the reaction rates between Fe ions (Fe^{2+}, Fe^{3+}) and OH^- in solution; this, in consequence, leads to the formation of smaller Fe_3O_4 NPs.

The setting times of C-PMMA and C-REA50 had been measured in our previous work,[8] that is, 750 ± 60 s for C-PMMA and 750 ± 30 s for C-REA50, which are in the range of that needed in ISO5833 ranging from 3 to 15 min.[23] The peak temperatures for samples C-PMMA and C-REA50 fully setting were reported to be 95 and 75°C, respectively, which

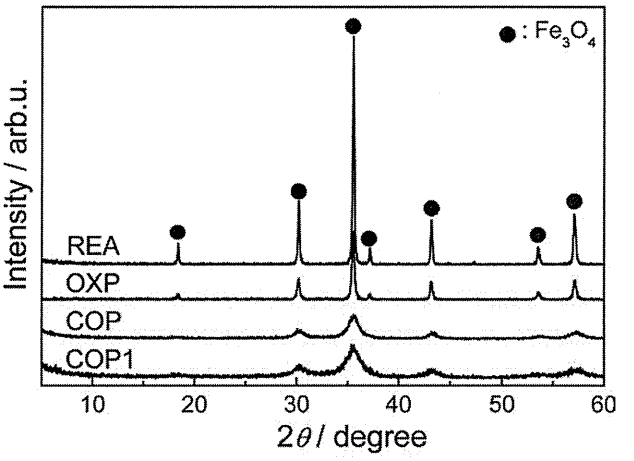

FIGURE 2. The XRD powder diffraction patterns of the magnetite powders used in this study.

TABLE II. Saturation Magnetizations (*Ms*'s) and Coercive Forces (*Hc*'s) of the Obtained Cement Samples Measured by VSM, in Comparison with Those of the Starting Fe_3O_4 Powders

Samples	Ms (emu g^{-1})	Hc(Oe)
REA	86.9	140.0
OXP	78.5	99.3
COP	43.9	14.2
C-REA50	45.7	141.1
C-REA30	25.8	140.3
C-OXP50	36.7	140.5
C-COP30	15.0	15.5

are similar to the peak temperatures of commercially available cement samples.[24] However, further works are still needed to confirm the setting times and peak temperatures of all other cement samples.

Table II lists the saturation magnetizations (*Ms*'s) and coercive forces (*Hc*'s) of the obtained cement samples measured in a magnetic field up to 10,000 Oe by VSM; they were compared with those of the starting Fe_3O_4 powders. *Ms*'s of C-REA50, C-REA30, C-OXP50, and C-COP30 were 45.7, 25.8, 36.7, and 15.0 emu g^{-1}, respectively, while *Hc*'s of C-REA50, C-REA30, C-OXP50, and C-COP30 were 141.1, 140.3, 140.5, and 15.5 Oe, respectively. The Fe_3O_4 contents (wt %) were evaluated from the ratio of *Ms* of the cement sample to that of the corresponding starting Fe_3O_4 powder, which was almost consistent with the initial mixing weight percent ratios of Fe_3O_4. The cements C-REA50, C-REA30, and C-OXP50 as well as their corresponding Fe_3O_4 powders (REA and OXP) exhibited large *Hc*'s, thereby indicating their ferromagnetic properties, while COP and C-COP30 had very small *Hc*'s, which suggests that COP and C-COP30 had superparamagnetic properties. These results indicate that there were no significant changes in the magnetic properties of the Fe_3O_4 NPs before and after their incorporation into the PMMA matrix.

Figure 3 shows the magnetization curves of the cement samples measured in magnetic fields up to 300 Oe and 120 Oe by VSM at room temperature. Figure 3(a) shows that for the magnetic field of 300 Oe, C-OXP50 and C-REA50 produced hysteresis loops with wide areas, whereas their loop areas significantly decreased when the field strength decreased to 120 Oe [Fig. 3(b)]. C-COP30 samples exhibited no obvious loops under both magnetic field conditions. The heat-generating ability of Fe_3O_4 NPs due to their hysteresis loss under AC magnetic fields can be estimated by integrating the area of the hysteresis loop.[12] Therefore, it can be inferred that remarkable heat is generated by C-OXP50 and C-REA50 by their hysteresis losses in the magnetic field of 300 Oe, but the generated heat significantly decreases for 120 Oe. Note that the heat generation of C-COP30 due to its hysteresis loss is not available because of its superparamagnetic properties.

In vitro heat studies

Figure 4 shows the changes in the surface temperatures of the cement samples in an AC magnetic field as a function of time. In a magnetic field of 300 Oe, the surface temperature of C-PMMA did not increase (not shown in Fig. 4), whereas the temperatures of C-OXP50, C-REA50, and C-REA30 increased rapidly to over 80°C within several tens of seconds, while the temperature of C-COP30 increased to 55°C within 250 s [see Fig. 4(a)]. The surface temperatures of C-OXP50, C-REA50, C-REA30, and C-COP30 reached 52, 49, 34, and 32°C, respectively, within 500 s in a magnetic field of 120 Oe. Moreover, the temperature for C-OXP50 increased more rapidly than that for C-REA50 under both magnetic field conditions.

For C-OXP50 and C-REA50, the increasing trends of surface temperatures are consistent with the trends for the area sizes of the hysteresis loops in the magnetic field of 300 Oe [see Figs. 3(a) and 4(a)]; this suggests that the heat generation by both cement samples can be primarily attributed to their hysteresis losses. In the magnetic field of 120 Oe, the temperature increases in all the samples slowed significantly in accordance with the predictions from the obtained hysteresis loop areas. This can be explained by the fact that the magnetic field is too weak to continue domain wall motions in the multi-domain Fe_3O_4 NPs distributed in C-REA50 and C-REA30; moreover, reorienting the magnetic moment in the single-domain Fe_3O_4 NPs distributed in C-OXP50 and C-COP30 becomes difficult under the same

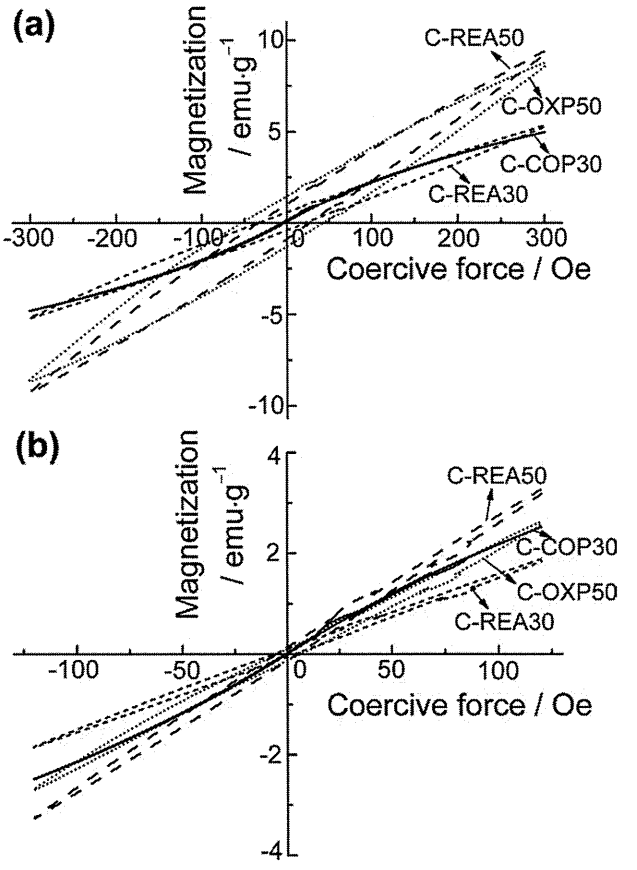

FIGURE 3. The magnetization curves of the cement samples measured in magnetic fields up to (a) 300 Oe and (b) 120 Oe by VSM at room temperature.

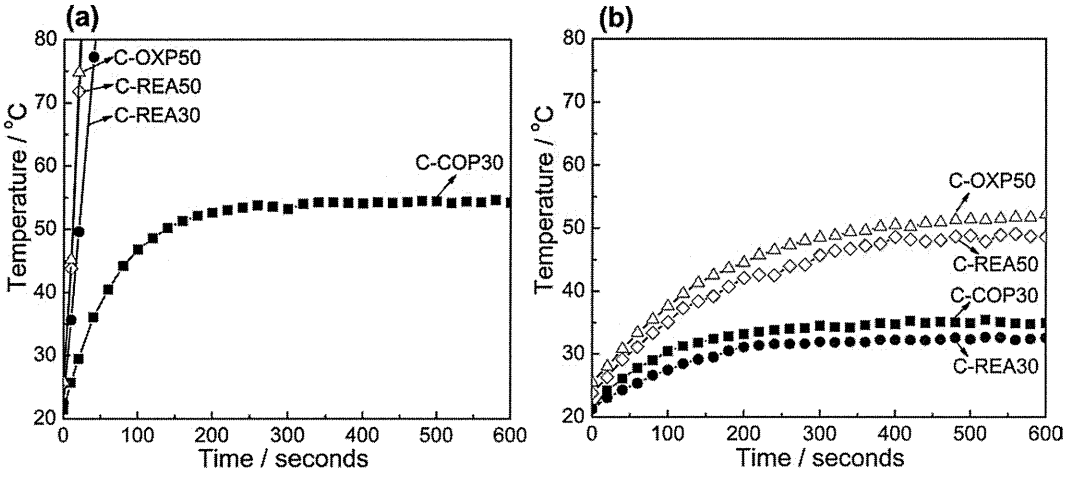

FIGURE 4. Changes in the surface temperature of samples in AC magnetic fields of (a) 300 Oe and (b) 120 Oe at a frequency of 100 kHz.

conditions. The heat generation in C-COP30 was mainly due to its Néel relaxation loss.[14]

Figure 5 shows the changes in the surface temperatures of the cement samples measured in a magnetic field of 40 Oe and frequency of 600 kHz. Within 600 s, the surface temperatures for C-COP30, C-OXP50, C-REA50, and C-REA30 increased by 77.2, 75.0, 60, and 40°C, respectively. The temperature increases in all the cement samples at 600 kHz were higher than those measured in the magnetic field of 120 Oe and 100 kHz [see Figs. 4(b) and 5]. This indicates that not only hysteresis loss, which contributed the heat generation in C-OXP50, C-REA50, and C-REA30, but also the relaxation loss, which contributed the heat generation in C-COP30, was significantly improved when the field frequency was increased to 600 kHz. In particular, C-COP30 containing superparamagnetic nanoparticles exhibited the highest temperature increase at 600 kHz, thereby demonstrating that it is more effective to improve the Néel relaxation loss of magnetic nanoparticles by increasing the field frequency; note that the Brown relaxation loss is unavailable here because magnetite NPs were fixed in the cement. For C-OXP50, which primarily contained single-domain ferromagnetic nanoparticles, the hysteresis loss determined by magnetocrystalline anisotropy primarily contributed to the heat generation.

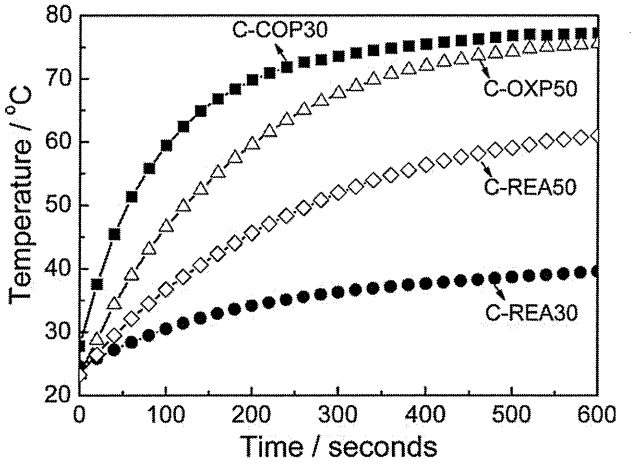

FIGURE 5. Changes in the surface temperature of samples in an AC magnetic field of 40 Oe at a frequency of 600 kHz.

The Néel loss is caused by the relaxation of the magnetization vector rotations of single-domain magnetic NPs in an AC magnetic field, which is a result of the gradual alignments of the magnetic moments during the magnetization process. The Néel relaxation time is given by

$$\tau = \frac{\sqrt{\pi}\tau_0 \exp(KV/kT)}{2\sqrt{KV/kT}} \quad (1)$$

Here k is Boltzmann's constant; K, anisotropy constant ($K = 1.35 \times 10^4$ J m^{-1}); τ_0, time constant ($\tau_0 \sim 10^{-9}$ s); T, temperature ($T = 293$ K); and V, nanoparticle volume (in m^3).[25] The loss power P corresponding to the Néel relaxation is approximated by

$$P = \frac{V(M_S H\omega\tau)^2}{2\tau kT(1+\omega^2\tau^2)} \quad (2)$$

Here M_S is the saturation magnetization (in emu g^{-1}); H, amplitude of the AC magnetic field (in Oe); and ω, the angular frequency of the AC field (s^{-1}).

Eq. (2) gives the maximum loss when $\omega\tau \cong 1$ at a critical volume size.[26] At our frequency, $\omega/2\pi = 100$ kHz, the relaxation time given by Eq. (1), the calculated nanoparticle size for P to reach a maximum is $d_1 = 17$ nm. Similarly, the calculated nanoparticle size is $d_2 = 15.5$ nm at a frequency of 600 kHz. Figure 6 shows the dependence of the nanoparticle size on the loss power due to the Néel relaxation calculated using Eqs. (1) and (2) for the field frequency used. As observed in Figure 6, there is a very sharp maximum in the loss power corresponding to a certain nanoparticle size distribution at different frequencies. C-COP30 contained small nanoparticles (11.5 ± 3.6 nm) that are closer to the range of the nanoparticle size distribution at 600 kHz, and therefore, it exhibited a higher heating efficiency in the magnetic field of 600 kHz.

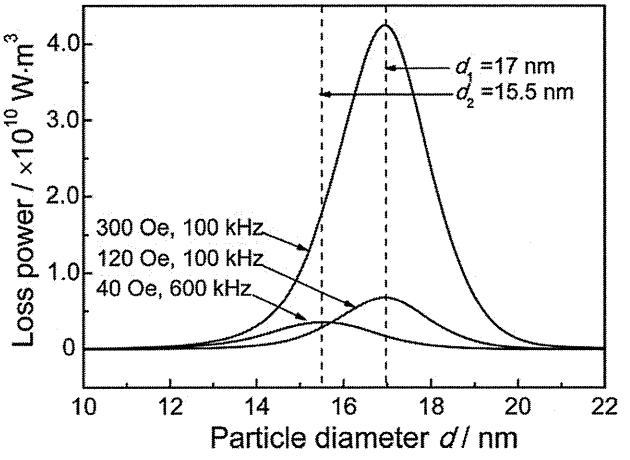

FIGURE 6. Loss powers due to the Néel relaxation in magnetite nanoparticles, which are calculated from Eqs. (1) and (2) as a function of the diameter of the particle, *d*.

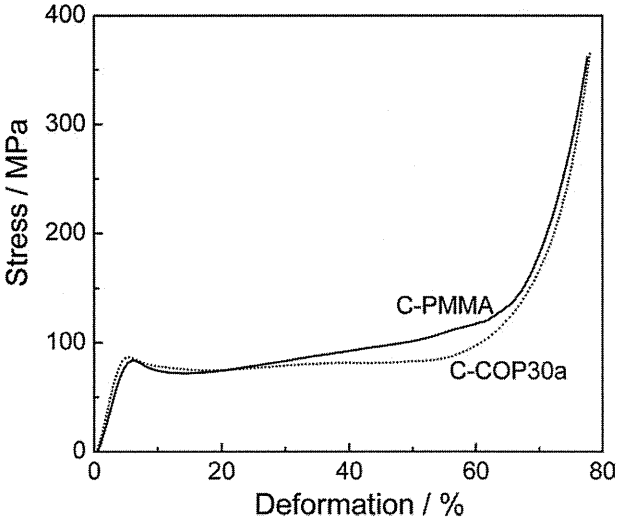

FIGURE 8. The stress–stain curve obtained from the compression tests of cement samples with and without the incorporation of Fe_3O_4 nanoparticles.

The actual heat generation of a sample is not proportional to the area of the hysteresis loop measured in a static applied magnetic field, because the large hysteresis loop of a sample is probably not formed in the applied AC magnetic fields because of the limitations to the field amplitude. Bone cement-containing magnetite NPs with a size distribution for achieving maximum loss power (see Fig. 6) under the applied magnetic field exhibited significant heating abilities due to their relaxation losses.

Mechanical properties

Figure 7 shows the compressive strength of C-PMMA and C-COP30a. The compressive strength was 83.5 ± 2.1 MPa for C-PMMA and 86.0 ± 2.6 MPa for C-COP30a; thus, they meet the criterion listed in ISO 5833 (≥70 MPa). Statistical analyses showed no significant differences between the compressive strengths of the cement samples with and without the incorporation of Fe_3O_4 NPs ($P > 0.05$). The slight decrease in the compressive strength exhibited by C-PMMA can be explained in terms of less powder content, which acts as reinforcements.[27]

Figure 8 shows the stress–stain curves obtained from the compression tests of cement samples. C-COP30a revealed similar mechanical behaviors as those of C-PMMA during the compression process. These results suggest that the incorporation of Fe_3O_4 NPs into cement by 30 wt % did not cause significant changes in the mechanical properties. These cements have sufficient mechanical strength for clinical applications as bone cement.

Residual monomer content in cement samples

Figure 9 shows the released content of residual monomer per gram of cements: C-PMMA and C-COP30a measured by liquid chromatography. The obtained results showed that

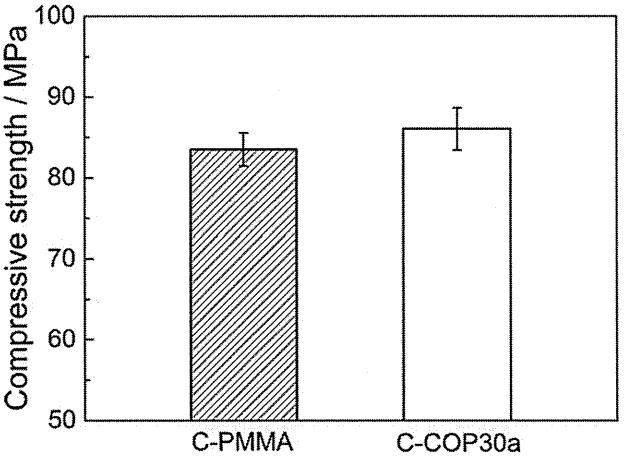

FIGURE 7. The compressive strength of cement samples with and without the incorporation of Fe_3O_4 nanoparticles. Data are shown as the mean ± SD ($n = 5$). $p > 0.05$ indicates no significant differences observed between the compressive strengths of both types of cement samples.

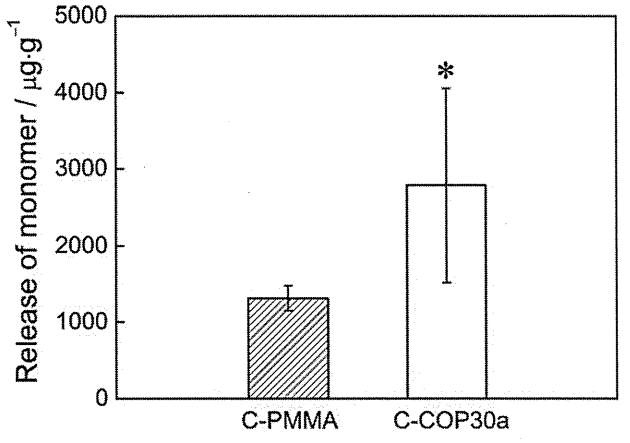

FIGURE 9. The released content of residual monomer per gram of cements: C-PMMA and C-COP30a measured by liquid chromatography. Data are shown as the mean ± SD ($n = 5$). The differences between the two columns were analyzed with the Student's *t* test. *$p < 0.05$ versus C-PMMA.

the monomer content in the eluate derived from sample C-COP30a was significantly higher than that from C-PMMA ($P < 0.05$). These results can be explained by taking into account that the higher powder proportion used in C-COP30a produces a mixture with higher initial viscosity and lower monomer content by volume unit, thereby inhibiting the polymerization reaction of the MMA monomer. This result is consistent with that reported by Vallo *et al.* who demonstrated a high ratio of liquid/powder leading to high degrees of monomer conversions when the PMMA bone cement was prepared by conventional methods by mixing liquid and powder components.[27] Some previous studies revealed that in the proportion of the components, the PMMA nanoparticles present in the cement have insignificant effects on the maximum conversions attained by the MMA monomer[27,28]; hence, the high residual monomer content in C-COP30a can be primarily attributed to the presence of Fe_3O_4 NPs.

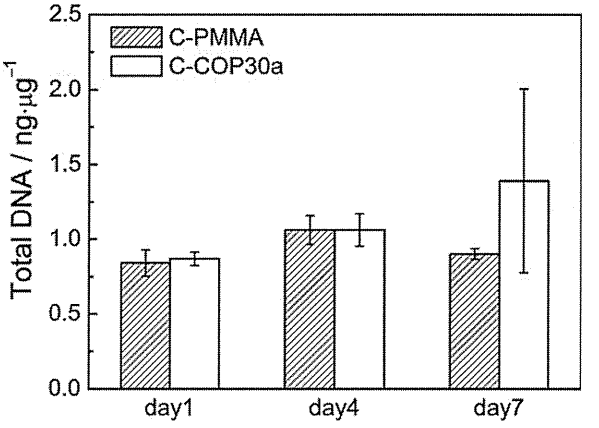

FIGURE 10. The total DNA concentration of Rat-1 fibroblast cells adhered on cement discs. Data are shown as the mean ± SD ($n = 5$). $p > 0.05$ indicates no significant increases in the DNA concentration measured until day 7 of the culture for both types of cement discs.

Biocompatibility evaluation

Cell proliferation is the very important feature of cytocompatibility of biomaterials. We utilized Rat-1 fibroblastic cell line since fibroblasts are representative of cells that will be encountered in the artificial implant environment. The attachment and adhesion belong to the first phase of cell/material interactions, and the quality of this first phase will influence the cell's capacity to proliferate on the implant.[29,30] DNA quantification test is a representative test for cell proliferation in the field of molecular cell biology. Therefore we employed DNA quantification test to assess cell proliferation on cement discs. In general, incubation of Rat-1 cells for 7 days should be enough to detect cell proliferation if the cells are in normal culture condition. In this study, the cell proliferation was examined after 1, 4, and 7 days of culture. Figure 10 shows the DNA concentrations of Rat-1 fibroblast cells cultured on cement discs of C-PMMA and C-COP30a. No significant increases in the DNA concentration were observed until day 7 of the culture for both types of cement discs ($P > 0.05$). This demonstrates the inhibitory effects of cement discs on the proliferation of Rat-1 cells. The Rat-1 cell line used in this study has been demonstrated to be able to proliferate vigorously in the same medium (DMEM) without cement discs in it after a 7-day incubation by another cell culture trial (data not shown).

The inhibitory effects of cements on the cell proliferation could be due to the toxicity from the released MMA monomer in the medium.[31] C-COP30a released higher MMA monomer content in the medium, which can be inferred from the data of Figure 9, and thus, lower DNA concentrations should be obtained for cell cultured on cement C-COP30a. In fact, no significant differences in the DNA concentrations were observed for both types of cement discs, and therefore, incorporating a certain amount of Fe_3O_4 NPs in cements probably acts positively on the proliferation of Rat-1 cells. In addition, higher ratios of PMMA, BPO, and DMPT had been used on the preparation of C-PMMA cements, and hence, their effects (maybe negative) on cell proliferation should be considered.

Although Fe_3O_4 NPs have previously been reported to be toxic to cells when its concentrations are more than 0.05 mg L^{-1},[9,10] in this study, it is possible that the Fe_3O_4 NPs contents released into the medium were too low to cause significant inhibitory effects on cell proliferation. Moreover, the embedded NPs in hard materials might have less toxicity than the well-dispersed NPs in fluids because of their less directed interactions with mammalian cells.

CONCLUSIONS

In this study, PMMA-based cements containing Fe_3O_4 NPs with different diameters were prepared and their *in vitro* heat studies were carried out in different AC magnetic fields. The heat generation of cements was demonstrated to be strongly dependent on the size of the magnetic NPs used and the conditions of the applied magnetic fields. Cement-containing ferromagnetic Fe_3O_4 NPs (REA and OXP) generated sufficient heat in a magnetic field of 300 Oe at a frequency of 100 kHz, and hysteresis loss primarily contributed to the heat generation. On the other hand, the heating capability of cement-containing superparamagnetic Fe_3O_4 NPs (COP) was significantly improved when the magnetic field frequency was increased to 600 kHz. Considering the limitations of the field amplitude, bone cement-containing magnetic NPs with dimension distributions to allow Neél relaxation under the applied magnetic field exhibited high heating ability.

The compression tests showed that the incorporation of Fe_3O_4 nanoparticles into cement by 30 wt % did not significantly change the mechanical properties of cements. From the DNA analysis results, there were no significant inhibitory effects on cell proliferation attributable to the presence of Fe_3O_4 nanoparticles. The *in vitro* study by DNA analysis of cell proliferation might be insufficient to support our conclusions. Further research will be carried out to confirm our data presented in this study by additional tests: (i) quantification of the amounts of ATP to access the cell proliferation, (ii) investigation of cell cycle of the Rat-1 cells incubated on the C-PMMA or C-COP30a. Our investigations are useful for designing new PMMA/Fe_3O_4 bone cements with high

heating efficiencies and good biocompatibilities for tumor therapy in bone, especially those in the vertebrae. Moreover, such investigations are necessary to address the increasing number of bone diseases in ageing societies today.

REFERENCES

1. Hall SE, Criddle RA, Comito TL, Prince RL. A case-control study of quality of life and functional impairment in women with long-standing vertebral osteoporotic fracture. Osteoporos Int 1999;9: 508–515.
2. Lovi A, Teli M, Ortolina A, Costa F, Fornari M, Brayda-Bruno M. Vertebroplasty and kyphoplasty: Complementary techniques for the treatment of painful osteoporotic vertebral compression fractures. A prospective non-randomised study on 154 patients. Eur Spine J 2009;18(Suppl 1):S95–S101.
3. Garfin SR, Yuan HA, Reilley MA. Kyphoplasty and vertebroplasty for the treatment of painful osteoporotic compression fractures. Spine 2001;26:1511–1555.
4. Deramond H, Depriester C, Galimbert P, Le Gars D. Percutaneous vertebroplasty with polymethylmethacrylate technique, indications and results. Radiol Clin North Am 1998;36:533–546.
5. Matsumine A, Kusuzaki K, Matsubara T, Shintani K, Satonaka H, Wakabayashi T, Miyazaki S, Morita K, Takegami K, Uchida A. Novel hyperthermia for metastatic bone tumors with magnetic materials by generating an alternating electromagnetic field. Clin Exp Metastasis 2007;24:191–200.
6. Uchida A, Wakabayashi H, Okamura A, Matsumine A, Kususaki K. Metastatic bone disease: Pathogenesis and new strategies for treatment, J Orthop Sci 2004;9:415–420.
7. Takegami K, Sano T, Wakabayashi H, Sonoda J, Yamazaki T, Morita S, Shibuya T, Uchida A. New ferromagnetic bone cement for local hyperthermia. J Biomed Mater Res 1998;43:210–214.
8. Kawashita M, Kawamura K, Li Z. PMMA-based bone cements containing magnetite particles for the hyperthermia of cancer. Acta Biomater 2010;6:3187–3192.
9. Katsnelson B, Privalova LI, Kuzmin SV, Degtyareva TD, Sutunkova MP, Yeremenko OS, Minigalieva IA, Kireyeva EP, Khodos MY, Kozitsina AN, Malakhova NA, Glazyrina JA, Shur VY, Shishkin EI, Nikolaeva EV. Some peculiarities of pulmonary clearance mechanisms in rats after intratracheal instillation of magnetite (Fe_3O_4) suspensions with different particle size in the nanometer and micrometer ranges: Are we defenceless against nanoparticles? Int J Occup Environ Health 2010;16:508–524.
10. Mahmoudi M, Simchi A, Milani AS, Stroeve P. Cell toxicity of superparamagnetic iron oxide nanoparticles. J Colloid Interface Sci 2009;336:510–518.
11. Ito A, Kobayashi T. Introcellular hyperthermia using magnetic nanoparticles: A novel method for hyperthermia clinical application. Thermal Med 2008;24:113–129.
12. Atsumi T, Jayadevan B, Sato Y, Tohji K. Fundamental studies of hyperthermia using magnetic particles as thermoseed. I. Development of magnetic particles suitable for hyperthermia. J Magn Soc Jpn 2006;30:555–560.
13. Li Z, Kawashita M, Araki N, Mitsumori M, Hiraoka M, Doi M. Magnetite nanoparticles with high heating efficiencies for application in the hyperthermia of cancer. Mater Sci Eng C 2010;30:990–996.
14. Ma M, Wu Y, Zhou J, Sun Y, Zhang Y, Gu N. Size dependence of specific power absorption of Fe_3O_4 particles in AC magnetic field. J Magn Magn Mater 2004;268:33–39.
15. Li Z, Kawashita M, Araki N, Mitsumori M, Hiraoka M, Doi M. Preparation of magnetic iron oxide nanoparticles for hyperthermia of cancer in a $FeCl_2$-$NaNO_3$-NaOH aqueous system. J Biomater Appl 2011;25:643–661.
16. Kang YS, Risbud S, Rabolt JF, Stroeve P. Synthesis and characterization of nanometer-size Fe_3O_4 and γ-Fe_2O_3 particles. Chem Mater 1996;8:2209–2211.
17. Goto K, Tamura J, Shinzato S, Fujibayashi S, Hashimoto M, Kawashita M, Kokubo T, Nakamura T. Bioactive bone cements containing nano-sized titania particles for use as bone substitutes. Biomaterials 2005;26:6496–6505.
18. Kawashita M. Domi S, Saito Y, Aoki M, Ebisawa Y, Kokubo T, Saito T, Takano M, Araki N, Hiraoka M. In vitro heat generation by ferromagnetic maghemite microspheres for hyperthermic treatment of cancer under an alternating magnetic field. J Mater Sci Mater Med 2008;19:1897–1903.
19. Jeyadevan B, Atsumi T, Suto M, Kasuya R, Sato Y, Tohji K. Synthesis and characterization of magnetic iron oxide nanoparticles suitable for hyperthermia. Thermal Med 2009;25:43–52, in Japanese.
20. Xu C, Houck JR, Fan W, Wang P, Chen Y, Upton M, Futran ND, Schwartz SM, Zhao LP, Chen C, Mendez E. Simultaneous isolation of DNA and RNA from the same cell population obtained by laser capture microdissection for genome and transcriptome Profiling. J Mol Diagn 2008;10:129–134.
21. Shutoh Y, Takeda M, Ohtsuka R, Haishima A, Yamaguchi S, Fujie H, Komatsu Y, Maita K, Harada T. Low dose effects of dichlorodiphenyltrichloroethane (DDT) on gene transcription and DNA methylation in the hypothalamus of young male rats: Implication of hormesis-like effects. J Toxicol Sci 2009;34:469–482.
22. Leung GW, Vickers ME, Yu R, Blamire MG. Epitaxial growth of Fe_3O_4 (111) on $SrTiO_3$ (0 01) substrates. J Cryst Growth 2008;310: 5282–5286.
23. Mori A, Ohtsuki C, Sugano A, Kuramoto K, Miyazaki T, Tanihara M, Osaka A. Bioactive PMMA-based bone cement modified with methacryloxypropyltrimethoxysilane and calcium salts. J Ceram Soc Japan 2003;111:738–742.
24. Kühn KD. Bone Cements. Berlin: Springer; 2000. p 21–35, 141–148, 226–232.
25. Okawa K, Sekine M, Maeda M, Tada M, Abe M. Heating ability of magnetite nanobeads with various sizes for magnetic hyperthermia at 120 kHz, a noninvasive frequency. J Appl Phys 2006;99: 08H102.
26. Hergt R, Andrä W, d' Ambly CG, Hilger I, Kaiser WA, Richter U, Schmidt HG. Physical limit of hyperthermia using magnetite fine particles. IEEE Trans Magn 1998;34:3745–3754.
27. Vallo CI, Montemartini PE, Cuadrado TR. Effect of residual monomer content on some properties of a poly(methyl methacrylate)-based bone cement. J Appl Polym Sci 1998;69:1367–1383.
28. Balke ST, Hamielec AE. Bulk polymerization of methyl methacrylate. J Appl Polym Sci 1973;17:905–949.
29. Shtansky DV, Gloushankova NA, Sheveiko AN, Kharitonova MA, Moizhess TG, Levashov EA, Rossi F. Design, characterization and testing of Ti-based multicomponent coatings for load-bearing medical applications. Biomaterials 2005;26:290–924.
30. Anselme K. Osteoblast adhesion on biomaterials. Biomaterials 2000;21:667–681.
31. Kedjarune U, Charoenworaluk N, Koontongkaew S. Release of methyl methacrylate from heat-cured and autopolymerized resins: Cytotoxicity testing related to residual monomer. Aust Dent J 1999;44:25–30.

Solution Structure of Clostridial Collagenase H and Its Calcium-Dependent Global Conformation Change

Naomi Ohbayashi,[†‡] Takashi Matsumoto,[§] Hiroki Shima,[¶] Masafumi Goto,[¶‖] Kimiko Watanabe,[‖] Akihito Yamano,[§] Yasutake Katoh,[¶] Kazuhiko Igarashi,[¶] Youhei Yamagata,[**] and Kazutaka Murayama[†*]

[†]Graduate School of Biomedical Engineering, Tohoku University, Sendai, Japan; [‡]Faculty of Pharmacy, Iwaki Meisei University, Iwaki, Japan; [§]Rigaku Corporation, Akishima, Japan; [¶]Graduate School of Medicine, Tohoku University, Sendai, Japan; [‖]New Industry Creation Hatchery Center, Tohoku University, Sendai, Japan; and [**]Graduate School of Agricultural Science, Tokyo University of Agriculture and Technology, Tokyo, Japan

ABSTRACT Collagenase H (ColH) from *Clostridium histolyticum* is a multimodular protein composed of a collagenase module (activator and peptidase domains), two polycystic kidney disease-like domains, and a collagen-binding domain. The interdomain conformation and its changes are very important for understanding the functions of ColH. In this study, small angle x-ray scattering and limited proteolysis were employed to reveal the interdomain arrangement of ColH in solution. The ab initio beads model indicated that ColH adopted a tapered shape with a swollen head. Under calcium-chelated conditions (with EGTA), the overall structure was further elongated. The rigid body model indicated that the closed form of the collagenase module was preferred in solution. The limited proteolysis demonstrated that the protease sensitivity of ColH was significantly increased under the calcium-chelated conditions, and that the digestion mainly occurred in the domain linker regions. Fluorescence measurements with a fluorescent dye were performed with the limited proteolysis products after separation. The results indicated that the limited proteolysis products exhibited fluorescence similar to that of the full-length ColH. These findings suggested that the conformation of full-length ColH in solution is the elongated form, and this form is calcium-dependently maintained at the domain linker regions.

INTRODUCTION

Clostridial collagenases are multimodular proteins consisting of three to five domains. The collagenases commonly contain a collagenase module, which is composed of activator and peptidase domains, at the N-terminal side and a collagen-binding domain (CBD) at the C-terminal end (1) (Fig. 1). Among the five collagenases, the collagenase from *Clostridium histolyticum*, ColH, has only one CBD, whereas the collagenase from *Clostridium botulinum*, ColB, possesses three CBDs. The other three collagenases, ColG from *C. histolyticum*, ColA from *Clostridium perfringens*, and ColT from *Clostridium tetani*, include two CBDs. Although ColT only consists of these two domain and module types (collagenase module and CBD), the other collagenases, except for ColH, include a polycystic kidney disease (PKD)-like domain, which may be involved in collagen recruitment (2). ColH includes two PKD-like domains, PKD1 and PKD2 (Fig. 1).

Intensive structural analyses of the individual domains of ColG and ColH have been conducted. The first crystal structure was reported for the CBD of ColG (3). The CBD structures were solved with calcium ions (holo form) and without calcium ions (apo form). The crystal structure of the collagenase module of ColG was recently determined (4) and revealed that bacterial collagenolysis proceeds by a chew-and-digest mechanism, in which the structural changes of the collagenase module, were suggested to involve open and closed conformations. Although a structural analysis was performed for the region from Tyr-119 to Gly-790, containing the collagenase module and the PKD-like domain, the position of the PKD-like domain was not exactly located in the crystal structure (4). The structure of the PKD-like domain was determined and discussed by the same group in a subsequent report (2). In addition to these structures, the crystal structures of the CBD of ColH have been deposited in the Protein Data Bank (PDB-IDs: 3JQW and 3JQX) (5). The sequence identities among the individual domains of ColH and ColG were calculated using ClustalW (6). The results showed that they are well conserved: 48% for the collagenase modules; 40–50% for the PKD-like domains; and 29–34% for the CBDs.

Calcium ions play a critical role in the enhancement of the interactions between collagens and collagenases (7,8). Furthermore, the binding mode of the CBD to the collagen triple-helix was proposed, based on NMR titration and small angle x-ray scattering (SAXS) studies (3,9). Ca^{2+} ion binding to collagenases contributes to the interactions with collagen and the stability of the CBD (3,10). In addition, Ca^{2+} ions reportedly play very important roles in the interdomain flexibility and thermal stability of full-length ColH, and are reversibly regulated (11).

The molecular mechanisms of the individual domains of collagenases have been investigated, in terms of both their structures and functions. However, the structure of

Submitted August 25, 2012, and accepted for publication February 14, 2013.

*Correspondence: kmura@bme.tohoku.ac.jp

Editor: Lois Pollack.

0006-3495/13/04/1538/8 $2.00

http://dx.doi.org/10.1016/j.bpj.2013.02.022

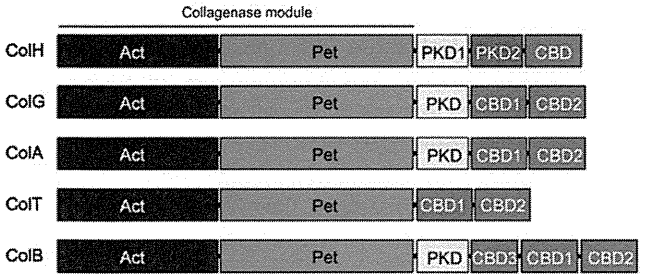

FIGURE 1 Domain architectures of clostridial collagenases. The five collagenases are ColH and ColG of *C. histolyticum*, ColA of *C. perfringens*, ColT of *C. tetani*, and ColB of *C. botulinum*. The domain notations are Act, activator domain; Pet, peptidase domain; PKD, polycystic kidney disease-like domain; CBD, collagen-binding domain.

the collagenase molecule, as a multidomain protein, remains poorly characterized. Here, we report the structural characterization of full-length ColH in solution. For the structural analysis of biological macromolecules in solution, SAXS is an important and useful approach (12–15). The ab initio beads model of ColH indicated that the overall conformation adopted a tapered form, with the longest dimension of ~140 Å. Under calcium-chelated conditions (with EGTA), the structure was further elongated. A limited proteolysis analysis indicated that the sensitivity to the protease was significantly increased under the calcium-chelated conditions. Fluorescence measurements suggested that a calcium-dependent conformational change occurred in the collagenase module. To our knowledge, this is the first investigation of the solution structure of full-length ColH and its calcium-dependent conformational change.

MATERIALS AND METHODS

Protein expression and purification

The protein sample was prepared as previously described (11). Briefly, ColH was expressed in *Escherichia coli* strain BL21(DE3) as a secreted form, and was subsequently purified using a Ni-NTA superflow (Qiagen, Hilden, Germany) column. The eluted protein was then subjected to MonoQ and Superdex 200 gel filtration chromatography (GE Healthcare, Little Chalfont, United Kingdom). The peak fractions were pooled and concentrated in 20 mM HEPES buffer (pH 8.0), containing 100 mM NaCl and 1 mM $CaCl_2$, to a final concentration of 11.0 mg/mL.

SAXS measurements

SAXS data were collected using a BioSAXS-1000 system equipped with an FR-E+ rotating anode x-ray generator (Rigaku, Akishima, Japan). The protein samples were prepared at concentrations of 1, 5, and 10 mg/mL with a calcium-containing buffer, and 10 mg/mL with a buffer containing 2 mM EGTA. The wavelength, λ, was 1.54189 Å (CuKα), and the sample-detector distance was 500 mm, leading to scattering vectors, q, that ranged from 0.009 to 0.65 $Å^{-1}$ with $q = (4\pi/\lambda)\sin\theta$, where 2θ is the scattering angle. The protein solutions or buffer (30 μL) were placed in a quartz capillary with a diameter of 1.0 mm, and the exposure time was 15 min/frame. The total exposure times for the calcium-containing conditions were 120 min for the 5 and 10 mg/mL solutions, and 240 min for the 1 mg/mL solution. For the EGTA-containing conditions, the total exposure times were 180, 240, and 360 min for the 10, 5, and 2 mg/mL solutions, respectively. The scattering images were processed with SAXSLab installed in the BioSAXS system (Rigaku), and the scattering intensities from the buffer solution were subtracted with PRIMUS (16). The forward scattering, $I(0)$, and the radius of gyration, R_g, were estimated using the Guinier approximation in the ATSAS program package (17). The $P(r)$ distributions were calculated from the scattering data for the 10 mg/mL solution with GNOM (18), by applying perceptual criteria for the estimation of D_{max}.

Ab initio and rigid body modeling

Ab initio modeling of the scattering envelopes was performed with GASBOR (19). The calculated resolution range was $0.009 < q < 0.60$ $Å^{-1}$. Eight individual reconstructions were calculated and averaged using DAMAVER (20). ColH domain models were prepared by SWISS-MODEL (21), using the crystal structures of ColG (collagenase module: 2Y3U; PKD-like domain: 3JS7) as the templates, except for the CBD. For the model of the CBD, PDB-ID: 3JQW was used. The closed conformation model for the collagenase module was manually built, as proposed in the collagen processing model (4), before homology modeling by SWISS-MODEL. Whole rigid body model construction was conducted for the ab initio beads model under the conditions with calcium, using these individual domain models. Before the BUNCH calculation, the domain models were aligned sequentially from the collagenase module to the CBD, with appropriate distances corresponding to the missing amino acids in the domain linker regions. The final ColH model was constructed by BUNCH (22) in the User mode with scattering data of $q < 0.2$, and was corrected manually. During the BUNCH calculations, distance restraints were used (2–3 Å/missing amino acid in the initial models). The theoretical scattering curve from the final model was calculated by CRYSOL (23). The ColH model was fitted to the beads model by SUPCOMB (24).

Limited proteolysis and electrospray ionization mass spectrometry

A ColH solution (1 mg/mL) was prepared in 20 mM HEPES (pH 8.0), 100 mM NaCl, 1 mM $CaCl_2$, in the presence or absence of 2 mM EGTA. Limited proteolysis was performed with lysyl endopeptidase (Lys-C; Sigma, St. Louis, MO) at an enzyme/substrate ratio of 1:200 (w/w) at 30°C. In the time course experiments, Lys-C proteolysis was stopped at 0, 2, 6, 10, 20, and 30 min by the addition of phenylmethylsulfonyl fluoride (final concentration, 1 mM). For the C-terminal fragment analysis, the ColH solution was digested by Lys-C for 30 min at 30°C as described previously, and then treated with carboxypeptidase B (16 units/mL) for 10 min at 30°C. The partially hydrolyzed products were separated by sodium dodecyl sulfate-polyacrylamide gel electrophoresis (SDS-PAGE). The bands on the SDS-PAGE gel were excised, placed in individual sample tubes, and subjected to in-gel trypsin digestion for 20 h at 37°C. The digested peptides were loaded onto a 75-μm fused silica capillary column containing C18 resin. The peptides were eluted with an acetonitrile gradient (typically 2.5–40%) in 0.1% formic acid, and analyzed by an LTQ Orbitrap XL mass spectrometer (Thermo Fisher Scientific, Waltham, MA).

Size exclusion chromatography and fluorescence measurements of the limited proteolysis products

A ColH solution (11 mg/mL) with 2 mM EGTA was hydrolyzed by Lys-C at 1:1,000 (w/w) at 30°C for 60 min. The partially hydrolyzed products were separated by size exclusion chromatography on a Superdex 200 column (GE Healthcare). The buffer conditions were the same as those in the purification process. The fractions containing the protein corresponding to the

100-kDa band on the SDS-PAGE gel were pooled and reapplied to the Superdex 200 column, to estimate the molecular mass under two different buffer conditions (with and without 2 mM EGTA). To prepare the 80 kDa band protein, a ColH solution was hydrolyzed as described previously, although for 180 min. The hydrolyzed products were separated by ion-exchange chromatography (ResourceQ, GE Healthcare) to purify the 80 kDa band protein. The fluorescence of both partially hydrolyzed products (100 and 80 kDa band proteins) was measured using an F-2500 spectrofluorometer (Hitachi, Tokyo, Japan) at 25°C. Fluorescence spectra were measured with an excitation wavelength of 492 nm, with emission from 500 to 650 nm. The excitation and emission bandwidths were both set at 10 nm. The ColH samples were mixed with freshly diluted SYPRO Orange (Invitrogen, Carlsbad, CA) (1:1000, v/v) under three different conditions: 1), with intact buffer; 2), with 2 mM EGTA; and 3), with additional 2 mM $CaCl_2$ added after 2 mM EGTA. The measurements were performed three times.

RESULTS

Overall conformation of ColH

To evaluate the overall structure, ColH was subjected to a SAXS analysis in the calcium-containing buffer (buffer-Ca: 20 mM HEPES (pH 8.0), 100 mM NaCl, and 1 mM $CaCl_2$) and buffer-Ca with 2 mM EGTA (buffer-Ca/EGTA: 20 mM HEPES (pH 8.0), 100 mM NaCl, 1 mM $CaCl_2$, and 2mM EGTA) (Fig. 2 *a*). The free Ca^{2+} concentration in the buffer-Ca/EGTA was estimated as 3.95 nM (pCa 8.4) by CHELATOR (25). Protein aggregation complicates the interpretation of scattering curves. The ratios of the forward scattering intensity to the concentration ($I(0)/c$) were comparable for the three concentrations (1 (or 2), 5, and 10 mg/mL) with buffer-Ca and buffer-Ca/EGTA (Table 1), suggesting that concentration or time-dependent aggregation did not occur. The SAXS analysis provides two important parameters for evaluating molecular size in solution: the radius of gyration, R_g, as the mean molecular size; and the maximal intermolecular dimension, D_{max}. The Guinier plots indicated that R_g was 37.9 Å in buffer-Ca and 39.1 Å in buffer-Ca/EGTA (Fig. 2 *b*). The $P(r)$ distributions were estimated by an indirect Fourier transformation of the intensity data (Fig. 2 *c*). The D_{max} values were calculated to be 138 Å in buffer-Ca and 184 Å in buffer-Ca/EGTA, from the $P(r)$ profile of ColH. Both SAXS parameters were increased by calcium chelation with EGTA. The low resolution ab initio model building was conducted using GASBOR (19). Fig. 3 *a* shows the ab initio beads models in buffer-Ca and buffer-Ca/EGTA. Under both buffer conditions, the overall shape of ColH was an elongated form with a swollen head region that tapered off toward the end. The longest dimension of ColH was further extended by calcium chelation with EGTA, as shown in the calculation of D_{max}. The dimensions of the swollen head regions were estimated to be ~90 × 45 Å and 70 × 70 Å in buffer-Ca and buffer-Ca/EGTA, respectively. On the other hand, the widths of the tapered end were 20–30 Å under both conditions.

Rigid body model construction fitted to SAXS data

To construct the domain arrangement of ColH, the known structures of the individual domains of clostridial collagenases were used. The rigid body model was built using homology-modeled structures (collagenase module (activator and peptidase domains) and two PKD-like domains of ColG) and the CBD of ColH. The crystal structure of the ColG collagenase module is the open form (4). However, the conformation of the open form did not fit the beads model of ColH in buffer-Ca, because the width of the open form of the collagenase module is ~115 Å, whereas that of the beads model is 90 Å. The approximate dimensions of the closed form of the collagenase domain are 85 × 60 Å, which fit the beads model dimensions well (Fig. 4 *a*). Considering the two structural variations of the collagenase module, the closed form of the collagenase module was adopted for modeling. The final rigid body model fit well to the beads model in buffer-Ca (Fig. 4 *b*). The modeled structure lacked structural information for the domain linker regions. These regions were Gly-721 to Ser-726 (between the peptidase domain and

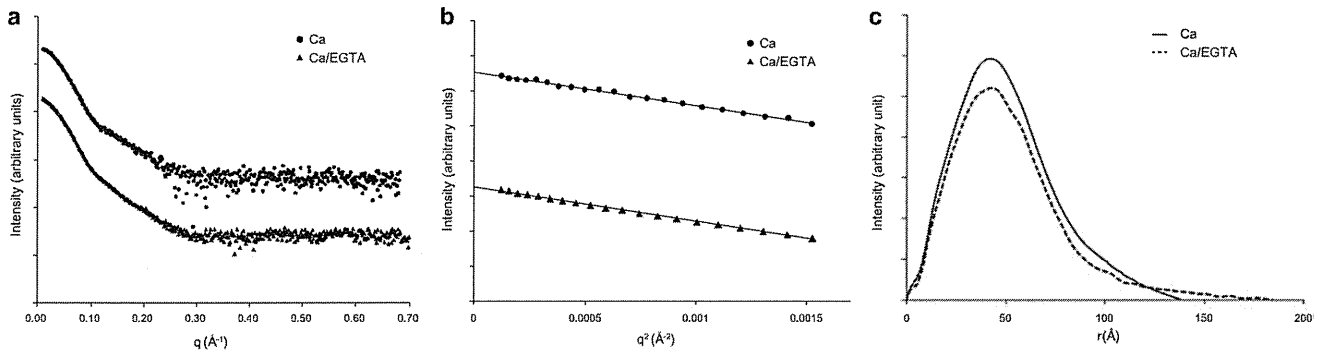

FIGURE 2 SAXS experiments. (*a*) Scattering data of ColH. The plots were vertically translated for clarity. (*b*) Guinier plot of a 10 mg/mL solution of ColH. The triangles and squares indicate the plots in buffer-Ca and buffer-Ca/EGTA, respectively. The plots were vertically translated for clarity. (*c*) Distance distribution functions, $P(r)$, for ColH in buffer-Ca (*solid line*) and buffer-Ca/EGTA (*dashed line*).

TABLE 1 Overall SAXS parameters

Protein concentration	Guinier analysis	Indirect Fourier transformation			
c, mg/ml	R_g, Å	D_{max}, Å	R_g, Å	$I(0)$	$I(0)/c$
(Buffer-Ca)					
10	37.9 ± 0.5	138	39.2 ± 0.2	2.164 ± 0.01	0.216
5	37.2 ± 0.8	138	39.5 ± 0.4	1.109 ± 0.009	0.222
1	36.5 ± 1.1	130	37.2 ± 0.5	0.203 ± 0.003	0.203
(Buffer-Ca/EGTA)					
10	39.1 ± 0.1	184	41.4 ± 0.3	1.900 ± 0.004	0.190
5	39.1 ± 0.2	184	41.4 ± 0.4	0.954 ± 0.003	0.191
2	39.8 ± 0.4	184	44.8 ± 0.5	0.403 ± 0.003	0.202

the first PKD-like domain), Leu-811 to Lys-815 (between the first PKD-like domain and the second PKD-like domain), and Pro-901 to Val-902 (between the second PKD-like domain and the CBD). The domain linker regions were relatively short (see Fig. S1 in the Supporting Material). Therefore, each domain was able to contact the adjacent domain. Although the crystal structures of the full-length clostridial collagenases have not been solved, an entire model of ColG on collagen microfibrils has been proposed (2,4). A comparison of these models revealed the similarity between the overall structural characteristics.

The beads model in buffer-Ca/EGTA was a further elongated form. A conformational change induced by calcium chelation has been reported for the CBD of ColG (3,10) and full-length ColH (11). Superposition of the rigid body model in buffer-Ca and the beads model in buffer-Ca/EGTA revealed that an unfitted region existed around the collagenase module and the CBD (Fig. 3 *b*), suggesting its conformational change by the calcium chelation.

Cleavage sites in limited proteolysis

Limited proteolysis is a useful tool for detecting protein flexibility (26). The sensitivity to protease digestion differs significantly between folded regions and unfolded regions, such as flexible loops. In this study, Lys-C was used as the protease for the limited proteolysis analysis, because it is specific for lysine residues, which are distributed throughout the ColH sequence. This residue-specific protease has the advantage of producing homogeneous ends in the digested peptide fragments, and these homogeneous ends facilitate subsequent analyses because of the reduced variation in the fragments.

Protease digestion was hardly observed for ColH in buffer-Ca. In contrast, ColH in buffer-Ca/EGTA was rapidly digested into three main bands, as evaluated by SDS-PAGE (Fig. 5 *a*). To determine the cleavage sites, fragment analyses by mass spectrometry were performed, by calculating the ratio of the detected fragment number from the limited proteolysis to the nondigested protein. The plot of the ratio should be reduced to zero when the limited proteolysis products do not include the N- and/or C-terminal regions. The results revealed that the three main bands were fragments digested at the C-terminal region. The evaluated C-terminal ends were Lys-915, Lys-825, and Lys-724, respectively (Fig. S2). In the second band, some additional fragments were detected, with digestion positions at 872–881. The limited proteolysis products treated with carboxypeptidase B provided a fragment without the C-terminal lysine. Therefore, the fragment at the C-terminal end is a semitryptic fragment. Such fragments were also detected for the first and third bands on SDS-PAGE in Fig. 5 *a*, but not for the second band (Fig. S1). Consequently, the sites digested by Lys-C mainly correspond to the domain linker regions between the second PKD-like domain and the

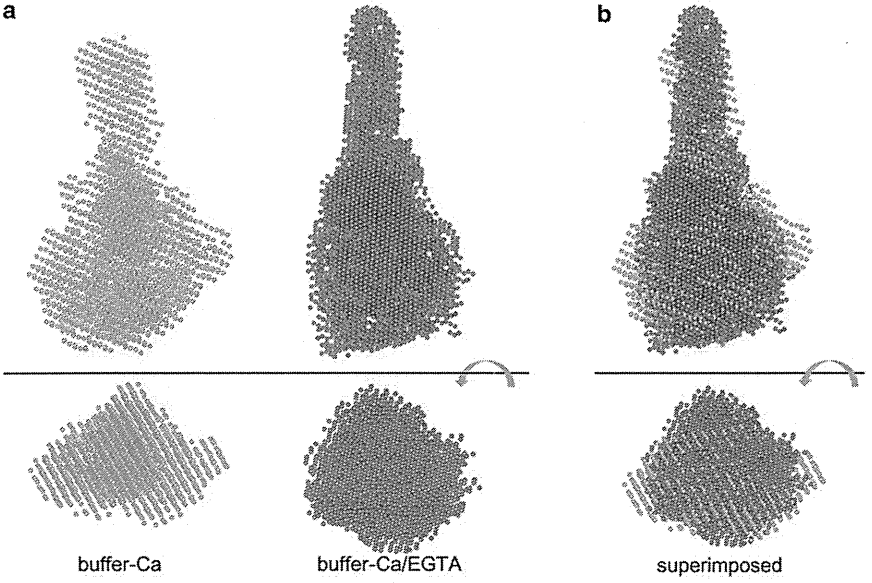

FIGURE 3 Comparison of the two ab initio beads models. (*a*) The beads models are represented in cyan for buffer-Ca and pink for buffer-Ca/EGTA. (*b*) A superimposed model with the beads models depicted in the same colors as in panel (*a*).

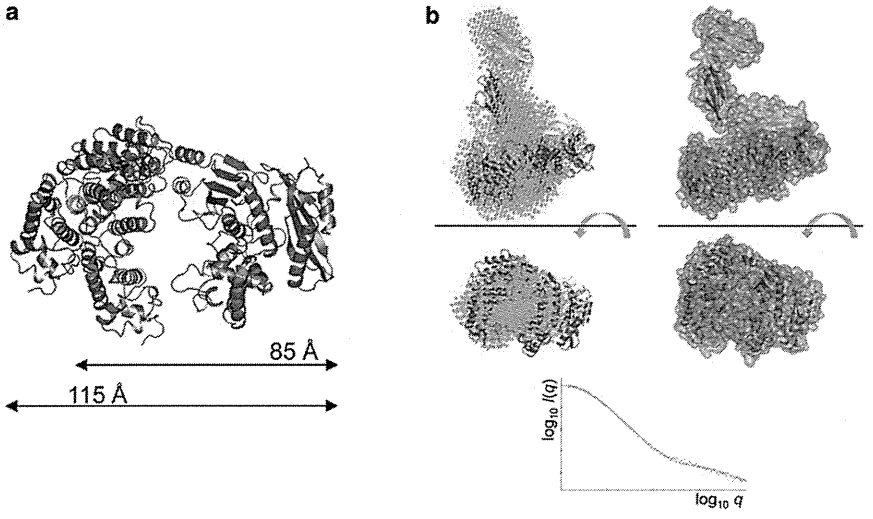

FIGURE 4 Model fitting between the ab initio beads model and the rigid body model. (*a*) Superimposed collagenase module conformations. The two conformations are superimposed on the peptidase domain. The activator domains of the conformations are colored blue (*solid*) and green (*open*). (*b*) Superimposition between the beads model in buffer-Ca and the rigid body model. (*Upper left panel*) The rigid body model is drawn as a ribbon representation and colored blue (collagenase module), yellow (PKD-like domain 1), magenta (PKD-like domain 2), and green (CBD). (*Upper right panel*) Surface representation of the rigid body model. (*Lower panel*) Evaluation of the modeled structure. The theoretical scattering curve was fitted to the SAXS data (*dots*).

CBD (Lys-915; ColHΔCBD) for the first band, the first PKD-like domain and the second PKD-like domain (Lys-825; ColHΔPKD-CBD) for the second band, and the collagenase module and the first PKD-like domain (Lys-724; ColHΔPKD-PKD-CBD) for the third band. According to the time course of the digestion pattern, the linker region between the second PKD-like domain and the CBD was clearly and significantly sensitive to digestion. On the other hand, the linker region between the first PKD-like domain and the second PKD-like domain was barely digested.

Analyses of the limited proteolysis products

The limited proteolysis products included three different domain-deleted ColH products, ColHΔPKD-PKD-CBD, ColHΔPKD-CBD, and ColHΔCBD. Among these products, ColHΔPKD-PKD-CBD and ColHΔCBD were purified by size exclusion chromatography (Fig. 5 *b*). Size exclusion chromatography of the purified ColHΔCBD revealed different elution volumes between the running buffers, i.e., 14.06 mL with buffer-Ca and 13.87 mL with buffer-Ca/EGTA (Fig. 5 *c*).

ColH reportedly shows fluorescence with the dye SYPRO Orange under the calcium-chelated conditions (11). This observation suggested that the interdomain conformation of ColH can be stabilized by hydrophobic interactions, because a fluorescent dye like SYPRO Orange binds to hydrophobic regions on the molecular surface (27). Fluorescence measurements were conducted for the fractions eluted from the size exclusion chromatography, to investigate the shortened domain constructions of ColH. The fluorescence enhancements of ColHΔCBD and ColHΔPKD-PKD-CBD were similar to that of the full-length protein (Fig. 5 *d*).

DISCUSSION

The crystal structure of the collagenase module of ColG was determined as the open form (4). The longest dimension of the collagenase module spans 115 Å, which is too wide to fit the beads models under both buffer conditions (buffer-Ca and buffer-Ca/EGTA), assuming the proposed domain alignment (4). Considering reasonable model dimensions, the closed form was adopted to fit the beads model. The collagenase module is composed of activator and peptidase domains, and these two domains are connected by a flexible glycine-rich hinge in ColG. No special secondary structural element was assigned for the corresponding part in ColH in the PSIPred (28) analysis. Therefore, the linker region between the activator domain and the peptidase domain of ColH is probably flexible. The closed form may be more stable than the open form in solution, because the N-terminal part of the activator domain and the putative loop region between Ser-529 and Phe-535 of the peptidase domain can interact. Consequently, the collagenase module of ColH predominantly adopts the closed form in solution.

The SAXS analysis revealed that ColH adopted a tapered shape under both conditions; i.e., in buffer-Ca and buffer-Ca/EGTA. In a comparison of the two beads models, the beads model in buffer-Ca/EGTA was more elongated (Fig. 3). Calcium ions reportedly play a critical role in maintaining the conformation of full-length ColH (11). In addition, the details of the calcium-dependent structural change have been reported for the CBDs of ColG (3,10,29) and ColH (5). The crystal structure of the CBD of ColH has also been determined for the calcium-binding form (PDB-ID: 3JQW) (5). The calcium-binding sites are spatially shared in both CBDs, suggesting that the calcium-dependent structural change of the CBD of ColH can occur in the same manner as that of ColG. According to the limited proteolysis analysis, the first digestion occurred at position Lys-915, which is the domain linker region between the second PKD-like domain and the CBD. The results suggested that the shape elongation of full-length ColH in buffer-Ca/EGTA includes a structural

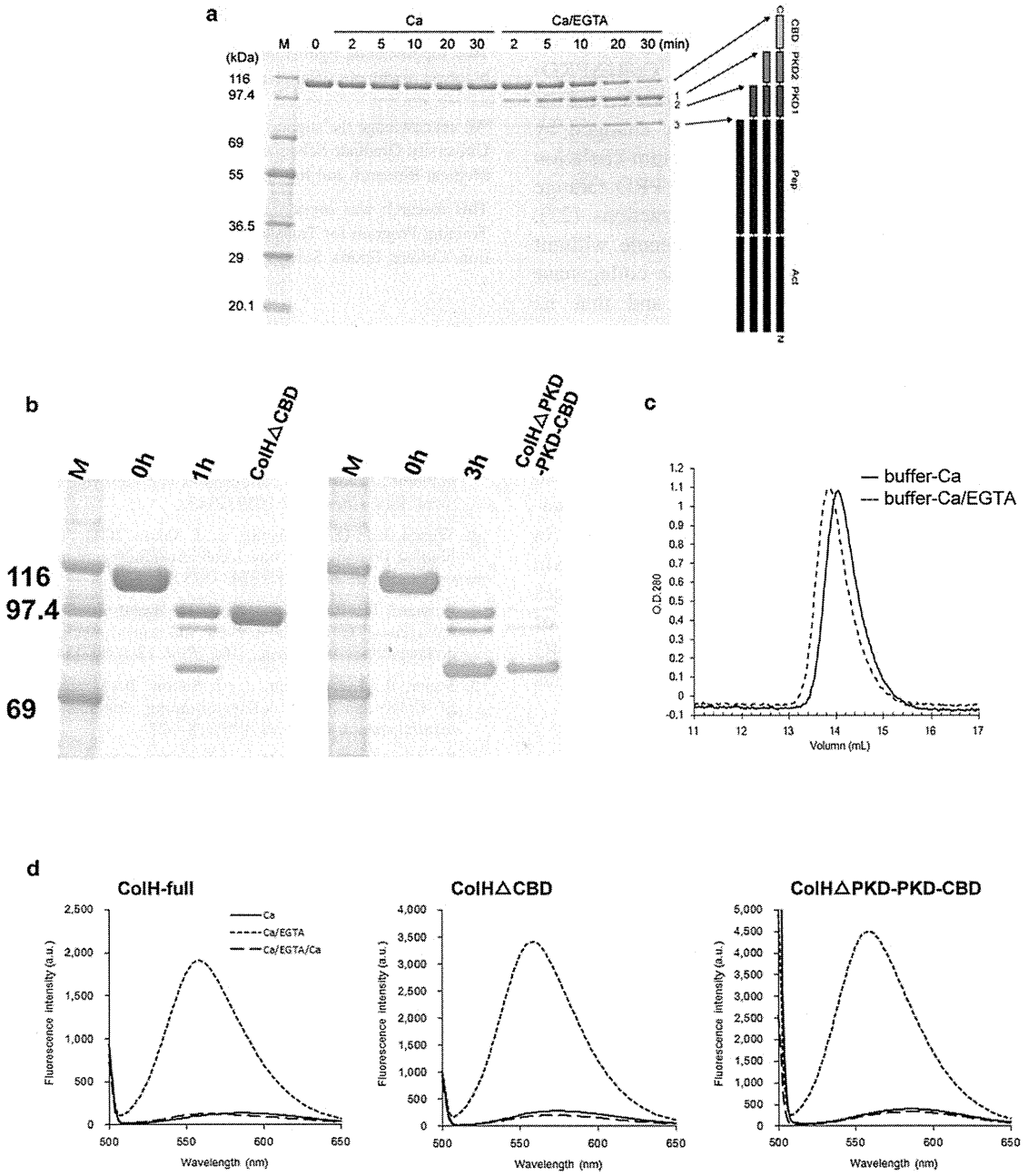

FIGURE 5 Limited proteolysis analyses. (*a*) SDS-PAGE analysis of the time course of the limited proteolysis products. The presumed C-terminal positions are indicated by arrows. M: protein standard markers. (*b*) SDS-PAGE of two limited proteolysis products. (*c*) Size exclusion chromatography of the C-terminal-deleted product ColHΔCBD under the two buffer conditions. (*d*) Fluorescence measurements of the limited proteolysis products. Solid line: without protein; long dashed line: in buffer-Ca/EGTA; short dashed line: after the addition of 2 mM $CaCl_2$ to the buffer-Ca/EGTA (buffer-Ca/EGTA/Ca). Left panel: full-length ColH; middle panel: C-terminal-deleted product, ColHΔCBD; right panel: C-terminal-deleted product, ColHΔPKD-PKD-CBD.

change at the linker region between the second PKD-like domain and the CBD.

The size exclusion chromatography analysis of ColHΔCBD indicated that the elution peak position with calcium was later than that with EGTA. This phenomenon was also found for the elution volumes of full-length ColH (11). The conformational change induced by calcium chelation with EGTA may reduce the interactions between the protein molecules and the matrix of the chromatography column, suggesting a calcium-dependent structural change of ColHΔCBD.

The limited proteolysis products were separated, and fluorescence measurements with the dye SYPRO Orange were conducted for the C-terminal-deleted products,

ColHΔPKD-PKD-CBD and ColHΔCBD. The separated C-terminal-deleted products showed similar fluorescence enhancement to that of full-length ColH. ColHΔPKD-PKD-CBD is identical to the collagenase module, and its calcium-dependent fluorescence is reversibly changed by the addition of excess calcium ions after calcium-chelation by EGTA. Fluorescence with a dye like SYPRO Orange indicates the existence of hydrophobic interactions (27). These results suggested that the ColH molecule without the CBD and the PKD-like domains; i.e., the collagenase module, includes calcium-binding site(s), and that its conformation may be maintained by hydrophobic interactions and calcium ion(s). Actually, about five calcium ions can bind to the entire ColH region (30). Two calcium ions are assigned to the CBD (3), and one ion is expected to bind to the PKD-like domain (2). Thus, at least four calcium ion-binding sites can be assigned on the ColH molecule to date. The fluorescence measurements indicated the possibility of a calcium-dependent conformational change in the collagenase module. Although it is difficult to explain how the conformation of the collagenase module changes upon calcium chelation, open/closed changes are one of the possibilities, because the crystal structure of the ColG collagenase module-PKD was determined under conditions without calcium (4).

CONCLUSIONS

In this study, a SAXS analysis was conducted to investigate the structural basis of the conformational change of full-length ColH induced by calcium chelation. The overall conformation of ColH is the tapered form under both buffer conditions. Although the crystal structure of the collagenase module of ColG is the open form, the collagenase module of ColH in solution with calcium predominantly adopts the closed form. The closed form will be more stable, as a consequence of interdomain interactions between the activator domain and the peptidase domain in solution.

We previously reported that the interdomain flexibility is predominantly and reversibly maintained by Ca^{2+} (11). In a comparison of the ab initio beads models under the two conditions (with buffer-Ca and buffer-Ca/EGTA), a more elongated structure was observed under the calcium-chelated conditions. The main conformational change will occur in the domain linker regions, especially the linker region between the second PKD-like domain and the CBD. The analysis of the limited proteolysis products suggested that the conformation of the collagenase module can be maintained in a calcium-dependent manner. Although the calcium-binding site on the collagenase module has not been determined thus far, further studies will be undertaken to investigate the molecular mechanism of the conformational change of the collagenase module.

SUPPORTING MATERIAL

Two supplemental figures and their legends are available at http://www.biophysj.org/biophysj/supplemental/S0006-3495(13)00239-7.

We acknowledge the support of the Biomedical Research Core of Tohoku University, Graduate School of Medicine, and TAMRIC (Tohoku Advanced Medical Research and Incubation Center).

This research was supported in part by the Coordination, Support and Training Program for Translational Research from the Ministry of Education, Culture, Sports, Science and Technology, Japan.

REFERENCES

1. Bruggemann, H., S. Baumer, ..., G. Gottschalk. 2003. The genome sequence of *Clostridium tetani*, the causative agent of tetanus disease. *Proc. Natl. Acad. Sci. USA.* 100:1316–1321.
2. Eckhard, U., and H. Brandstetter. 2011. Polycystic kidney disease-like domains of clostridial collagenases and their role in collagen recruitment. *Biol. Chem.* 392:1039–1045.
3. Wilson, J. J., O. Matsushita, ..., J. Sakon. 2003. A bacterial collagen-binding domain with novel calcium-binding motif controls domain orientation. *EMBO J.* 22:1743–1752.
4. Eckhard, U., E. Schönauer, ..., H. Brandstetter. 2011. Structure of collagenase G reveals a chew-and-digest mechanism of bacterial collagenolysis. *Nat. Struct. Mol. Biol.* 18:1109–1114.
5. Bauer, R., J. J. Wilson, ..., J. Sakon. 2013. Structural comparison of ColH and ColG collagen-binding domains from *Clostridium histolyticum*. *J. Bacteriol.* 195:318–327.
6. Thompson, J. D., D. G. Higgins, and T. J. Gibson. 1994. CLUSTAL W: improving the sensitivity of progressive multiple sequence alignment through sequence weighting, position-specific gap penalties and weight matrix choice. *Nucleic Acids Res.* 22:4673–4680.
7. Matsushita, O., C. M. Jung, ..., A. Okabe. 1998. A study of the collagen-binding domain of a 116-kDa *Clostridium histolyticum* collagenase. *J. Biol. Chem.* 273:3643–3648.
8. Matsushita, O., T. Koide, ..., A. Okabe. 2001. Substrate recognition by the collagen-binding domain of *Clostridium histolyticum* class I collagenase. *J. Biol. Chem.* 276:8761–8770.
9. Philominathan, S. T., T. Koide, ..., J. Sakon. 2009. Unidirectional binding of clostridial collagenase to triple helical substrates. *J. Biol. Chem.* 284:10868–10876.
10. Philominathan, S. T., O. Matsushita, ..., J. Sakon. 2009. Ca2+-induced linker transformation leads to a compact and rigid collagen-binding domain of *Clostridium histolyticum* collagenase. *FEBS J.* 276:3589–3601.
11. Ohbayashi, N., N. Yamagata, ..., K. Murayama. 2012. Enhancement of the structural stability of full-length clostridial collagenase by calcium ions. *Appl. Environ. Microbiol.* 78:5839–5844.
12. Jacques, D. A., and J. Trewhella. 2010. Small-angle scattering for structural biology–expanding the frontier while avoiding the pitfalls. *Protein Sci.* 19:642–657.
13. Mertens, H. D., and D. I. Svergun. 2010. Structural characterization of proteins and complexes using small-angle X-ray solution scattering. *J. Struct. Biol.* 172:128–141.
14. Svergun, D. I. 2010. Small-angle X-ray and neutron scattering as a tool for structural systems biology. *Biol. Chem.* 391:737–743.
15. Schneidman-Duhovny, D., S. J. Kim, and A. Sali. 2012. Integrative structural modeling with small angle X-ray scattering profiles. *BMC Struct. Biol.* 12:17.
16. Konarev, P. V., V. V. Volkov, ..., D. I. Svergun. 2003. PRIMUS: a Windows PC-based system for small-angle scattering data analysis. *J. Appl. Cryst.* 36:1277–1282.

17. Petoukhov, M. V., P. V. Konarev, ..., D. I. Svergun. 2007. ATSAS 2.1 - towards automated and web-supported small-angle scattering data analysis. *J. Appl. Cryst.* 40:S223–S228.

18. Svergun, D. I. 1992. Determination of the regularization parameter in indirect-transform methods using perceptual criteria. *J. Appl. Cryst.* 25:495–503.

19. Svergun, D. I., M. V. Petoukhov, and M. H. J. Koch. 2001. Determination of domain structure of proteins from X-ray solution scattering. *Biophys. J.* 80:2946–2953.

20. Volkov, V. V., and D. I. Svergun. 2003. Uniqueness of ab initio shape determination in small-angle scattering. *J. Appl. Cryst.* 36:860–864.

21. Arnold, K., L. Bordoli, ..., T. Schwede. 2006. The SWISS-MODEL workspace: a web-based environment for protein structure homology modelling. *Bioinformatics.* 22:195–201.

22. Petoukhov, M. V., and D. I. Svergun. 2005. Global rigid body modeling of macromolecular complexes against small-angle scattering data. *Biophys. J.* 89:1237–1250.

23. Svergun, D., C. Barberato, and M. H. J. Koch. 1995. CRYSOL - a program to evaluate x-ray solution scattering of biological macromolecules from atomic coordinates. *J. Appl. Cryst.* 28:768–773.

24. Kozin, M. B., and D. I. Svergun. 2001. Automated matching of high- and low-resolution structural models. *J. Appl. Cryst.* 34:33–41.

25. Schoenmakers, T. J., G. J. Visser, ..., A. P. Theuvenet. 1992. CHELATOR: an improved method for computing metal ion concentrations in physiological solutions. *Biotechniques.* 12:870–874, 876–879.

26. Dokudovskaya, S., R. Williams, ..., M. P. Rout. 2006. Protease accessibility laddering: a proteomic tool for probing protein structure. *Structure.* 14:653–660.

27. Epps, D. E., and B. M. Taylor. 2001. A competitive fluorescence assay to measure the reactivity of compounds. *Anal. Biochem.* 295:101–106.

28. Buchan, D. W. A., S. M. Ward, ..., D. T. Jones. 2010. Protein annotation and modelling servers at University College London. *Nucleic Acids Res.* 38(Web Server issue):W563–W568.

29. Sides, C. R., R. Liyanage, ..., J. Sakon. 2012. Probing the 3-D structure, dynamics, and stability of bacterial collagenase collagen binding domain (apo- versus holo-) by limited proteolysis MALDI-TOF MS. *J. Am. Soc. Mass Spectrom.* 23:505–519.

30. Bond, M. D., and H. E. Van Wart. 1984. Characterization of the individual collagenases from *Clostridium histolyticum*. *Biochemistry.* 23:3085–3091.